Targeting retinal cell types by synthetic promoters in 3D stem cell derived-retinal organoids

Doctoral thesis
to obtain a doctorate (Dr. med.)
from the Faculty of Medicine
of the University of Bonn

Sijia Yan
from Meishan, China
2026

Written with authorization of
the Faculty of Medicine oft he University of Bonn

First reviewer: Prof. Dr. Volker Busskamp

Second reviewer: Prof. Dr. Marieta Toma

Day of oral examination: 09.01.2026

From the Clinic and Polyclinic for Ophthalmology

Table of contents

List of abbreviations

01F49i N B7 iPSC line	B7 cell line
ACs	Amacrine cells
AMASS	Agarose Microwell Array Seeding and Scraping
AMD	Age-related macular degeneration
ANOVA	Analysis of Variance
BCs	Bipolar cells
BGH pA	Bovine growth hormone polyadenylation
Blasti	Blasticidin
BMP	Bone morphogenic protein
BSA	Bovine serum albumin
Ca^{2+}	Calcium ion
cDNA	Complementary DNA
CRX	Cone-rod homeobox
DAPI	4',6-diamidino-2-phenylindole
$_{d}H2O$	Distilled water
DMEM	Dulbecco ‘s modified eagle medium
DNA	Deoxyribonucleic acid
DNA	Deoxyribonucleic acid
dNTP	Deoxyribonucleotide triphosphate
dpi	Day post induction
DPBS	Dulbecco’s phosphate buffered saline
E.coli	*Escherichia Coli*
EB	Embryoid bodies
EDTA	Ethylenediaminetetraacetic acid

EGFP	Enhanced green fluorescentprotein
ESC	Embryonic stem cells
FACS	Fluorescence-activated cell sorting
FBS	Fetal bovine serum
FGF	Fibroblast growth factor
GCL	Ganglion cell layer
GFP :	Green fluorescent protein
HCs	Horizontal cells
hESC	Human embryonic somatic cell
hiPSC	Human induced pluripotent stem cell
IHC	Immunohistochemistry
IGF-1	Insulin-like growth factor – 1
INL	Inner nuclear layer
IPL	Inner plexiform layer
ipRGC	intrinsically photosensitive RGC
iPSC	Induced pluripotent stem cell
IS	Inner segment
ITRs	Inverted terminal repeat sequences
K^+	Potassium
LCA	Leber congenital amaurosis
LGN	lateral geniculate nucleus
MG	Müller glia
Mg^{2+}	Magnesium
MgCl	Magnesiumchloride
mESC	mouse embryonic somatic cell
mRNA	Messenger RNA
Na^+	Sodium

NaCl	Sodium chloride
NADP	Nicotinamide adenine dinucleotide phosphate
NIM	Neural induction media
NSD	Normal donkey serum
ONL	Outer nuclear layer
OPL	Outer plexiform layer
OS	Outer segment
OV	Opticle vesicle
PB	PiggyBac
PBS	Phosphate buffer saline
POU4F1	Pit-Oct-Unc class 4 homeobox
PR	Photoreceptor
Puro	Puromycin
qRT-PCR	Real-Time Quantitative Reverse Transcription polymerase chain reaction
RGC	Retinal ganglion cell
RO	Retinal organoid
ROCKi	Rho Kinase inhibitor
RPE	Retinal pigment epithelium
RP	Retinitis pigmentosa
Rpm	Revolution per minute
SLC17A6	Solute carrier family 17 member
tdTomato	Tandem dimer tomato
TGF-β	Transforming growth factor beta
UBC	Ubiquitin c

1 Introduction

1.1 The human retina

The retina is a light-sensitive and about 200 µm thin tissue located at the posterior of the eye, crucial for converting photons into electrical signals that are delivered to the brain (Masland, 2012a). This tissue facilitates visual perception, allowing humans to interact with and interpret the world around them. The retinogenesis begins during embryonic development when the eye field region of the diencephalon differentiates into bilateral optic vesicles. These vesicles subsequently invaginate to form the optic cup, which then generates the retinal pigment epithelium (RPE) and the neural retina with its intricate lamellar architecture (Pearson, 1980). The mature retina comprises various neuronal and glial cell types. The retinal neuronal cells are rod and cone photoreceptors (PRs), retinal ganglion cells (RGCs), amacrine cells (ACs), bipolar cells (BCs), and horizontal cells (HCs). The most important non-neuronal cell is the Müller glial (MG), as known as the major type of glia cell in the retina. These cells are systematically arranged into three nuclear layers interspersed with two plexiform layers. The nuclear layers are the innermost ganglion cell layer (GCL) from RGC, the inner nuclear layer (INL) from ACs, BCs and HCs, and the outer nuclear layers (ONL) from PRs. The inner and outer plexiform layers (IPL/OPL) are the synaptic connections between retinal cells (Fig. 1). PRs are located adjacent to the RPE in the outermost layer. They detect photons and convert them into electrical signals leading to a hyperpolarization. The neuronal activity is transmitted to BCs, which serve as building blocks to generate raw materials for further visual processing in the next station by RGCs (Euler et al., 2014; Masland, 2012a; Wässle, 2004). The axons of RGCs group together to form the optic nerve, which delivers final visual signals from the retina through the thalamus to the visual cortex in the occipital lobe (Dhande and Huberman, 2014; Sanes and Masland, 2015). HCs and ACs are inhibitory interneurons that modulate retinal signaling. The HCs enhance visual contrast, and ACs specialize in detecting directional motion (Masland, 2012b). MGs are crucial in maintaining potassium homeostasis and

recycling neurotransmitters. They also form the inner blood-retinal barrier, thus ensuring optimal retinal functionality (Reichenbach and Bringmann, 2013). The RPE, situated adjacent to the PRs, constitutes the outer blood-retinal barrier. It is responsible for phagocytosing PR outer segments and recycling visual pigments. (Strauss, 2005).

The primate retina is divided into two distinct regions. The periphery exhibits low spatial acuity and plays a role in night vision and various aspects of motion perception (Surridge et al., 2003). The central retina, known as the fovea, features a one-to-one connection between cone via BC to RGC, facilitating high spatial acuity vision crucial for reading and face recognition (Bringmann et al., 2018). Since over 60 distinct retinal cell types have been identified and described by Masland (2012a), retinal cells are categorized into distinct classes, allowing for differentiation based on morphological, functional, and transcriptomic characteristics (Bae et al., 2018; Baden et al., 2016; Dacey et al., 2003; Macosko et al., 2015; Peng et al., 2019).

The retina is fragile and has a very limited capacity for self-renewal. Impairment of different types of retinal cells leads to loss of vision, which then impairs the quality of life of patients. Primary open-angle glaucoma is a worldwide prevalent neuropathy characterized by necrosis of RGCs due to increased intraocular pressure and is the main cause of irreversible blindness worldwide (Li et al., 2016). In the Western world, age-related macular degeneration (AMD) is considered the most common cause of visual impairment. According to a meta-analysis by Li et al. (2020), the number of people with AMD is estimated to increase from 67 million to 77 million by 2050. Retinitis pigmentosa (RP) is a genetically inherited, heterogeneous retinal dystrophy due to primary degeneration of PRs. The prevalence of RP is about 1 in 4,000 (Hamel, 2006). As glaucoma and AMD affect millions worldwide, effective therapeutic strategies have been developed for certain cases.

Early-stage glaucoma can be effectively treated with first-line medications and minimally invasive surgery, and the progression of wet age-related macular degeneration (AMD)

can be slowed down with anti-vascular endothelial growth factor injections. However, so far, there is no effective therapy for RP, glaucoma at a late stage, and other rare retinal dystrophies, and thus cell transplantation as a potential therapy comes into question. Consequently, a more comprehensive understanding is urgently required for the intricate retinal function and the precise mechanisms underlying retinal diseases.

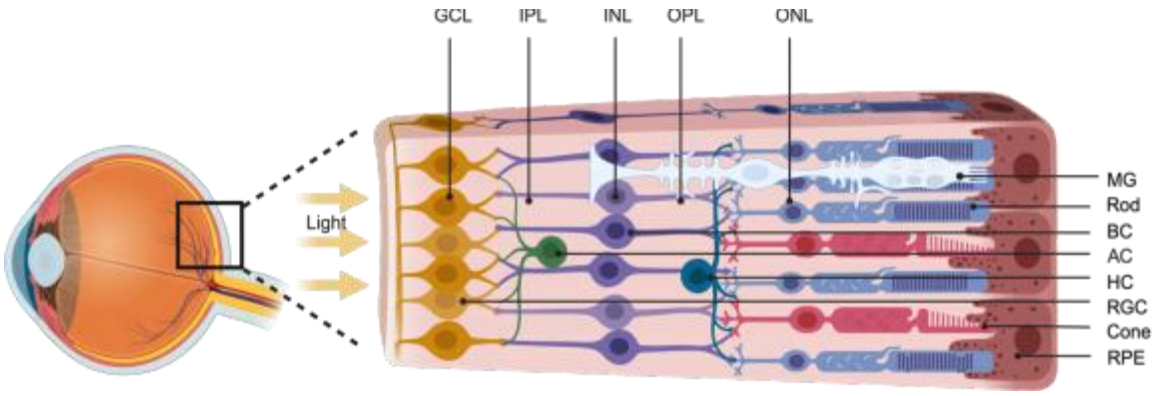

Fig. 1: Composition of retinal cells and nuclear and synaptic layers in the retina. The PRs receive the light stimuli, convert it into an electrical signal, and transmit it via bipolar cells and RGCs into the visual cortex. The image was generated by Biorender.com.

1.2 Induced pluripotent stem cells and their use in retinal research

In adults, stem cells are essential for tissue repair and regeneration in organs, and for example, are located in the liver and bone marrow (Esrefoglu, 2013; Undale et al., 2009). However, those stem cells in the liver and bone marrow have already possessed organized characteristics and functions, which means their differentiation potentials are restricted. In contrast, embryonic stem cells (ESCs) are derived from the inner cell mass of a blastocyst, which can differentiate into all three layers of the embryonic germ: the mesoderm, the ectoderm, and the endoderm. Because of their significant long-term self-renewal capabilities and the capacity to differentiate into various cell types, scientists investigated them to study organ development and diseases. Mouse embryonic stem cells (mESCs) and human embryonic stem cells (hESCs) demonstrated the ability to generate all cell types through *in vitro* development processes (Evans and Kaufmann,1981; Pera et al., 1989). The application of hESCs has proven to be a reliable and effective method for modeling human diseases. However,ethical concerns

regarding embryo disruption prompted the exploration of alternative methods. Therefore, another approach came into focus: reprogramming differentiated cells back to the pluripotent stem cells. In 2006, Takahashi and Yamanaka showed that adding four transcription factors (Oct4, Sox2, Klf4 and c-Myc) to mouse fibroblasts could turn them into pluripotent cells. This method was later used on human dermal fibroblasts (Takahashi et al., 2007). Human induced pluripotent stem cells (hiPSCs) exhibit characteristics similar to ESCs, including the expression of pluripotency markers and surface proteins and the capacity to differentiate into all three germ layers (Takahashi et al., 2007; Yu et al., 2007). This method facilitates the reprogramming of a patient's own cells, resulting in autologous induced pluripotent stem cells (iPSCs) suiTab. for cell transplantation as a personalized therapy, minimizing the risk of immune rejection owing to human leukocyte antigen compatibility (Nakatsuji et al., 2008).

Previously, studies of the retina have mostly relied on animal models rather than post-mortem human retinal tissue, because preservation of post-mortem retinal tissue requires rapid isolation and sustained oxygenation, making the process very time-consuming (Cowan et al., 2020; Fradot et al., 2011). Furthermore, the availability of donated post- mortem retinal tissues is restricted compared to animal models, and the disease status at the time of extraction is often not well defined. While animal models have improved our understanding of the retina's developmental, physiological, functional, and regenerative characteristics, challenges still remain. These include interspecies variations, as rodent models lack a macula and have only dichromatic vision, and ethical concerns associated with the use of non-primate animal models (Collin et al., 2020; Szatko et al., 2020). To address these issues, patient-derived iPSCs, which have the ability to differentiate into different cell types, including retinal cells, when introduced with appropriate fate specifying factors, are being used to study the human retina (Krohne et al., 2012). Researchers started to use two-dimensional (2D) adherent cell cultures such as iPSCs to grow cells in a monolayer, to mimic specific tissue characteristics in drug discovery, disease modeling, and cell replacement therapy. The hiPSCs were induced to

differentiate into retinal cells by the stepwise addition of growth factors and small molecules. The bone morphogenic protein (BMP) and transforming growth factor beta (TGF-β) signaling antagonists were employed to direct cells towards the forebrain, subsequently activating the retinal specification pathway via insulin-like growth factor-1 (IGF-1) signaling (Chamber et al., 2009; Lamba et al., 2006). In 2009, Meyer et al. successfully generated RPE and PRs that express cone-rod homeobox (CRX) from hiPSCs. Although 2D systems effectively produced different retinal cell types, exhibiting fundamental characteristics, they were limited by replicating the complex cell-cell interactions (Hirami et al., 2009; Lamba et al., 2006; O'Hara-Wright et al., 2020; Osakada et al., 2009). Three-dimensional retinal organoids (3D-ROs) derived from iPSCs, by contrast, present a stable and efficient model with enhanced cell-cell interaction to recapitulate the lamination structure and function of the retina in vitro (Eiraku et al., 2011; Nakano et al., 2012; Völkner et al., 2016; Zhong et al., 2014).

1.3 Introduction to 3D-retinal organoids and their applications

The concept of organoids originated in the 1980s, with early tissue culture models suggesting 3D cellular organization, such as the work on pulmonary alveoli by Sugihara et al. (1993). The first true organoids, which derived from stem cells that closely imitated the architecture and functionality of native human organs, emerged in the early 2000s. A landmark achievement occurred in 2009 when Sato et al. generated long-term cultured intestinal organoids from mouse stem cells, demonstrating the potential of organoid systems to model organ development and function *in vitro*. Since then, the field has rapidly advanced, resulting in various organ-specific models, including retinal organoids (ROs) by Eiraku et al. (2011), liver organoids by Huch et al (2013), and brain organoids by Lancaster et al. (2013), all derived from pluripotent stem cells. The generation of the first self-organized 3D ROs with stratified neuroepithelia was established by Eiraku and Sasai in 2011 using the floating serum-free embryoid body- like aggregates method. The EBs derived from mESCs were cultured in a modified serum-free culture, supplemented with Matrigel as an extracellular matrix and low-growth factors in

suspension. This induced a spontaneous formation of optic vesicles (OV), which, after lateral evagination, invaginated into the optic cup-like structures, thereby simulating embryonic retinogenesis *in vivo* and specifying the RPE and neural retina. This protocol was subsequently modified for hESCs and hiPSCs by integrating temporally regulated extrinsic factors such as Wnt or BMP antagonists for neural induction (Hallam et al., 2018; Kuwahara et al., 2015; Singh et al., 2015). Other small molecules were added subsequently into the cultures as refinement to improve the ROs maturation. For example, the fibroblast growth factor 1 (FGF1) was included to promote the maturation of PRs in ROs specifically (Brooks et al., 2019; Nakano et al., 2012). Retinal acid (RA) and taurine were also added to obtain a more structural lamination (Wagstaff et al., 2021; Wahlin et la., 2017; Zhong et la., 2014). Moreover, the incorporation of insulin-like growth factor -1 (IGF-1) facilitated PR maturation, as demonstrated by Mellough et al. (2015), and the application of hydrogels enhanced ROs yield (Hunt et al., 2017).

In 2014, Zhong et al. employed a combination of 2D and 3D methods for the first time, in contrast to the earlier 3D approach utilized by Nakano et al. (2012), this method bypassed the EB aggregation stage and involved plating early 3D aggregates onto laminin-coating to produce the OVs from adherent retinal cells. In this approach, it was found that 2 out of 13 randomly selected, 27-week-old, human-derived ROs demonstrated functional, light-responsive PRs for the first time; In 2018, Hallam et al. also produced PRs responding to light stimuli that can modulate their activity in the first few minutes. In subsequent years, the generation of ROs was further improved through refined chemical and material modification protocols. Material modification, through the implementation of pre-defined bioreactors and continuous oxygen supply, enhances oxygen flow and nutrient distribution while reducing necrosis within the RO. The process accelerated the differentiation of early developmental cell populations, resulting in high yields of mature PRs with cilia and OS-like structures appropriate for transplantation into mice (DiStefano et al., 2018; Ovando-Roche et al., 2018). Moreover, it enhanced RGC migration and maturation as well (Gao et al., 2016). The use of microfluidics in a retina-on-chip model to replicate the vascular

nutrition supply enhances differentiation efficiency (Achberger et al., 2019; Manafi et al., 2021).

Recent transcriptome profiling of ROs and the human retina has identified notable similarities, including cellular composition, lamination, and unique differentiation markers in developing ROs that correspond with those present in human retinas (Cowan et al., 2020; Sridhar et al., 2020). However, it was found that different iPSC lines concerning their competence in generating laminar retinal structures can impact the formation and quality of ROs (Cowan et al., 2020; Lowe et al., 2016).

In this study, the Agarose Microwell Array Seeding and Scraping (AMASS) protocol established by Cowan et al. (2020) was employed. A defined number of single cells were seeded into a 9 x 9 agarose microwell array, which initiated the self-formation of EBs. Different from other protocols, the AMASS method follows a 3D- to- 2D- to -3D approach, where the free-floating EBs (3D) were transferred to Matrigel-coated plates (2D) and provided with specific supplements and growth factors such as to facilitate the formation of optic cup-like structures (Fig. 2A; Fig. 9). At around W4, a checkerboard scraping technique was employed to release these optic cup-like structures into the medium, resulting in floating 3D-ROs (Fig. 2A). These ROs exhibited the ability to mature into a five-layered retinal structure, encompassing all retinal cell types and mature synapses that closely mimic *in vivo* retinogenesis. To note, the AMASS protocol facilitates the self-formation of EBs, especially with regulated sizes and a streamlined scraping technique. Overall, the AMASS protocol offers a reliable and reproducible approach for producing large batches of ROs with enhanced efficiency and optimized media use.

The current applications of the ROs are disease modeling, drug testing and cell transplantation studies (Fig. 2B). Utilizing patient-specific, disease-targeted 3D model systems enables the exploration of underlying mechanisms in heterogeneous retinal diseases such as RP, Leber congenital amaurosis (LCA), and Stargardt disease. For instance, Shimada et al. (2017) used patient-derived ROs with a CEP290 mutation for

LCA to mirror an early-onset retinal degeneration phenotype that was previously observed clinically. Similarly, Sharma et al. (2017) revealed pathophysiological deficits in autophagy associated with TRNT1-related RP, insights that are otherwise inaccessible in patients. The exploration of pathogenic splicing variants in the ABCA4 gene, linked to Stargardt disease, has also been documented (Khan et al., 2020). Furthermore, ROs facilitate the assessment of pharmacological effects on retinal dysfunction, such as the protective effects of 4-hydroxytamoxifen and diethylstilbestrol, as well as the retinotoxicity of moxifloxacin (Hallam et al., 2018; Ito et al., 2017). Additionally, ROs provide a promising avenue for harvesting cells in advanced transplantation studies. Gasparini et al. (2019) highlighted their utility in obtaining mature PRs with high specificity, while Oswald et al. (2021) also demonstrated the potential transplant viability of RGCs. Collectively, ROs represent an advanced and highly promising tool for future studies in retinal research.

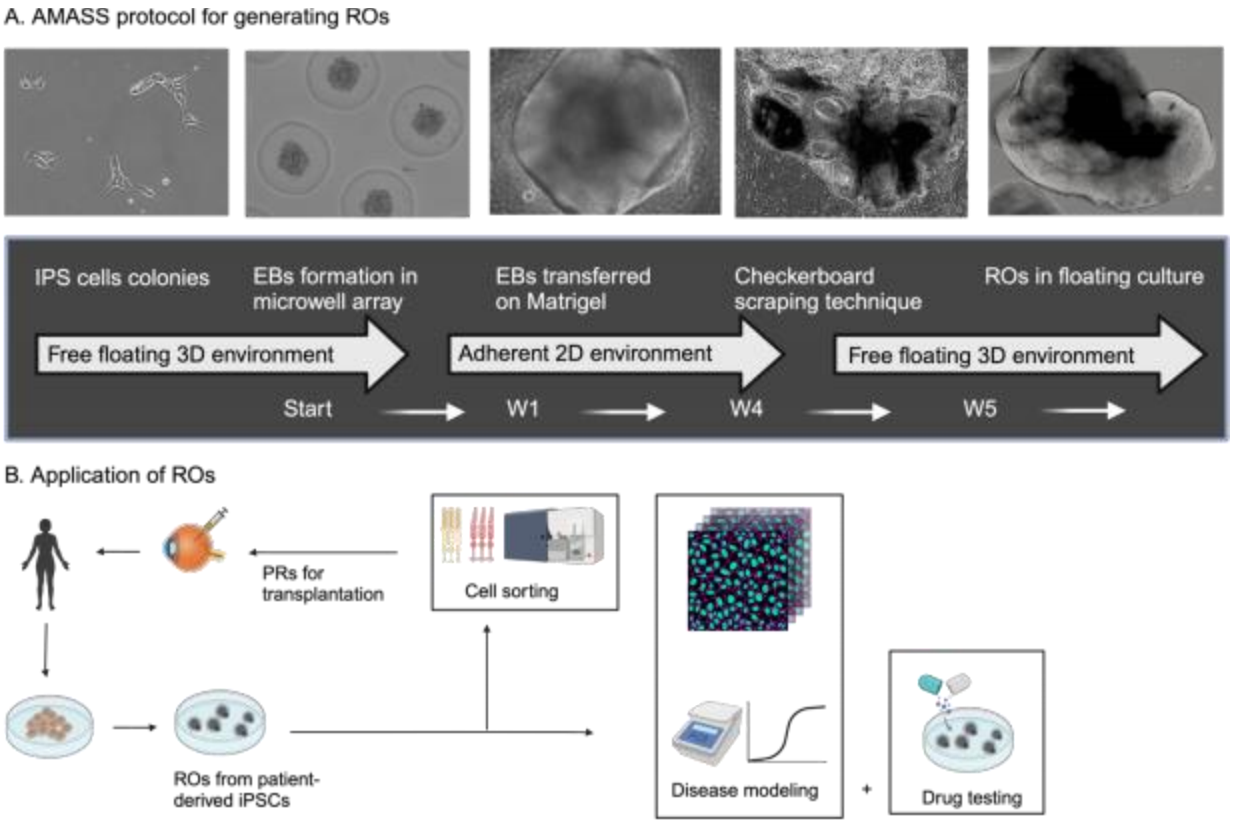

Fig. 2: A representation of the generation of ROs using the AMASS protocol as described by Cowan et al. (2020) and the current application of the ROs. A: The iPSC colonies are dissolved into single cells, which are then seeded into agarose microwells. The EBs are

formed by W1 and subsequently transferred onto Matrigel-coated plates, where they develop retinal structures. In order to create free-floating ROs, the checkerboard scraping technique is employed. B: The ROs derived from patient-specific iPSCs are able recapitulate the *in vivo* retinogenesis and serve thus as a more physiologically and functionally relevant model in disease modeling, drug testing and cell transplantation studies. Image created using Biorender.com

1.4 The retinal ganglion cells and cone photoreceptors

RGCs are the initial cell type to develop both *in vivo* and *in vitro* (Cepko et al., 1996; Lu et al., 2020; Rapaport et al., 2004; Wahle et al., 2023; Young, 1985) (Fig. 3c). They appear in the ROs around W6 and reach abundance by W12, while being almost entirely absent at W18 (Wahle et al., 2023). Their cell bodies are located in the innermost GCL of the retina, with extending axons embedded within the IPL. RGCs serve as the primary output neurons of the retina and generate an action potential (AP) that leads to the release of glutamate at their terminals.Kuffler's pioneering functional experiment(1953) categorized RGCs into two primary groups: ON and OFF. The study recorded the extracellular action potentials of RGCs in the mammalian retina using fine-tipped microelectrodes under various stimuli. It demonstrated that stimulation of the central receptive field elicited an ON response in certain RGCs and an OFF response in others, whereas stimulation of the surrounding area produced an opposing effect. Currently, the diversity of RGCs encompasses more than 30 distinct types identified within the mammalian retina (Masland, 2012a; Sanes and Masland, 2015). Each type of RGC reflects the result of a distinct visual computation executed by the retina (Gollisch and Meister, 2010). The initial classification relied on stratification levels and morphological characteristics (Badea and Nathans, 2004; Coombs et al., 2007). A combined classification of morphology, stratification level, functional characteristics, and projection pathway was described by Dacey et al. (2003) to achieve consensus in classification. Subsequently, the subtypes are distinguished by molecular and genetic characteristics (Baden et al., 2016; Dhande and Hubermann, 2014). Kim et al. (2021) recently summarized the known subtypes classified within each perspective (Fig. 3a). The Midget RGCs, representing 70 % of RGCs, are characterized by their small soma size

and receptive field (RF). They project in the parvocellular pathway in the lateral geniculate nucleus (LGN) and have a one-to-one connection with midget bipolar cells, which receive input from single cones, enabling fine spatial resolution, specific red-green chromatic opponency, and depth perception. Parasol RGCs make up about 10 % of all RGCs and are characterized by big soma size. They project to the magnocellular pathway in LGN and are optimized for detecting motion, flicker, and depth. They exhibit large RF and high contrast sensitivity but lack chromatic processing. Small bistratified RGCs, representing 5-8 % of RGCs, are a distinct subtype involved in shortwave color detection. The project in the koniocellular pathway of the LGN. Their dual dendritic stratification in the ON and OFF layers of the inner plexiform layer facilitates the excitatory input from ON bipolar cells initiated by S-cones and the OFF-light response from L+M-cone signals, enhancing chromatic contrast in visual processing. Lastly, the intrinsically photosensitive RGCs (ipRGCs) contribute 1 % of total RGCs, exhibiting large, sparse dendritic fields. Humans exhibit three known subtypes: M1, M2, and M4. The M1 subtype expresses melanopsin and receives inhibitory input from short-wavelength (S) cones, which are involved in the regulation of circadian rhythms. The M2 subtype plays a role in the blue cone pathway and regulates the pupillary light reflex. The ipRGCs are vulnerable in mitochondrial optic neuropathies such as leber hereditary optic neuropathy (LHON) and late-onset neurodegenerative disorders such as Alzheimer's and glaucoma (Cui et al., 2015). In general, due to the lack of ability to self-renew, the RGCs can be easily affected under circumstances leading to irreversible vision loss.

At molecular level, there are few common pan-RGC markers such as the transcription factor from Pit-Oct-Unc class 4 homeobox *(POU4F)* family, *Slc17a6* encoding the transporter Vglut2,surface protein Thy1 and the RNA-binding protein with multiple splicing (RBPMS) (Badea and Nathan., 2004; BarnsTab. and Dräger, 1984; Rodriguez et al., 2014; Tran et al., 2019). Some specific gene expressions can deliver clustering of

subtypes, such as the *OPN4* encoding the melanopsin and Tbr2, a T-box-containing transcription factor, specific markers for ipRGCs (Mao et al., 2014; Peng et al., 2019; Yan et al., 2020.).

PRs that capture photons and convert them into electrical signals are crucial for both photopic and scotopic vision. The cones develop following the RGCs at approximately week 12, which is earlier than the emergence of rods at around week 18 (Lu et al., 2020; Wahle et al., 2023) (Fig. 3c). Primates exhibit trichromatic vision, in contrast to rodents (Bowmarker and Hunt, 2006). The human cones are categorized into three types: L-cones with opsin one long-wave sensitive (OPN1LW), M-cones with opsin one medium-wave sensitive (OPN1MW), and S-cones with opsin one short-wave sensitive (OPN1SW) (Mustafi et al., 2009). L- and M-cones are mainly located in the fovea, arranged in a hexagonal pattern, with each cone linked to a single RGC, which contributes to the fovea's high visual acuity. S-cones comprise approximately 5 % of the total cone population, are predominantly located in the peripheral regions of the retina, and are absent from the center of the human fovea (Roorda et al., 2001). This is because higher-frequency photons (short-wave) are filtered by the pigments in the lens and macula, causing the absence of S-cones in the macula. It also reduces retinal damage and enhances image sharpness. Thus, the contribution to color vision primarily arises from L- and M-cones (Mustafi et al., 2009). Nonetheless, S-cones that detect blue light, working together with ipRGCs, play a role in the regulation of circadian rhythms.

At the molecular level, recoverin, a calcium binding protein located predominately in the outer segment (OS) of PRs, was identified in both cones and rods, serving as a specific marker for PRs (Kawamura, 1993; Keltner and Roth, 1993; Zang and Neuhauss, 2018). There is another protein that is specific to mammalian cones named Arrestin 3 (Krupnick and Benovic, 1998). The morphology of both cones and rods comprises five regions: OS, connecting cilium, inner segment (IS), nuclear region, and synaptic region (Fig. 3b). The OS serves as the primary component in phototransduction. The cilium serves as the primary cytoskeletal component of the OS in mature PRs and constitutes the sole cytoplasmic link between the IS and OS. The IS contains a significant number of mitochondria to fulfill its elevated energy requirements. The synaptic terminal of cones

demonstrates multiple synaptic contacts, facilitating communication with various bipolar and horizontal cells. This arrangement contributes to high-acuity and photopic vision, in contrast to rods, which possess single synaptic ribbons connecting to either bipolar cells or horizontal cells (Mustafi et al., 2009). In addition to this, there are several other distinct characteristics in cones. The cones contain opsins that facilitate color vision in light conditions, whereas rods utilize rhodopsin for scotopic vision in low-light conditions. The OS of cones is shorter and conical, with discs containing photopigments that are continuous with the plasma membrane, which contrasts with the discrete, stacked discs found in rods, allowing for rapid regeneration of photopigments and enhanced adaptation to varying light intensities (Fig. 3b). The cilium of cones is crucial as it serves as the primary pathway for transporting materials, including opsin synthesized in the IS, to the OS (Liu et al., 1999). Diseases associated with PR dysfunction, such as RP, LCA, and AMD, can lead to vision loss. Nevertheless, the main cause of clinically significant vision loss is cone degeneration. Although rod degeneration is the cause of RP, it leads to secondary cone degeneration (Shelley et al., 2009).

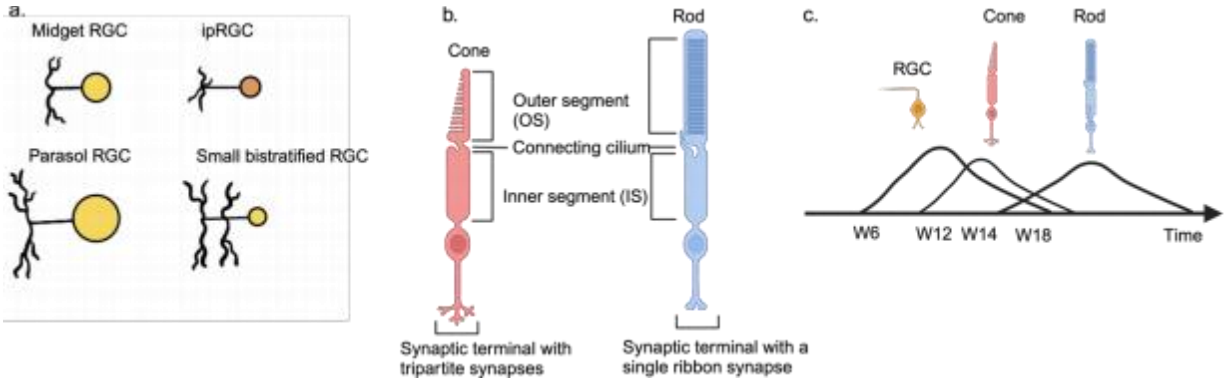

Fig. 3: Schematic drawing of morphology and the differentiation trajectory of RGCs and PRs. On the left (a) are subtypes of RGCs, including the Midget RGC, with a small soma and RF; the Parasol RGC, with a large soma and RF; the small bistratified RGC, which has dendrites in both the IPL and OPL; and the ipRGC responsible for circadian regulation and the pupillary reflex. (b) PRs have five parts including the OS, connecting cilium, IS, nucleus, and synaptic terminal. At the synaptic terminal, the cones synapse multiple times to both HCs and BCs whereas the rods synapse only once either to BCs or to HCs. To the right (c) is the differentiation time curve. The RGCs at appear first at week

6 while the cones appear second at W12. Then at W18 the rods appear. The image was generated by Biorender.com.

1.5 Current limitation of 3D-retinal organoids

Although retinal organoids (ROs) represent themselves as a more accurate model for studying human retinal diseases and yielding functional retinal cells, ROs face several drawbacks. Firstly, commonly using IHC, qRT-PCR, and single cell sequencing to confirm and analyze retinal cells in ROs at different time points are though concise but time-intensive and consume high numbers of ROs which is limited in each batch. Also, the retinal cells within ROs are so far not live tracked, meaning only downstream analysis could deduce the developmental status of retinal cells. Live cell imaging will be meaningful to provide us with a quick view and broad development of the retinal cells in living ROs. Secondly, a significant drawback is that the lack of vascularization system in the organoids restricts nutrient and oxygen supply, leading to limited size, core necrosis, and thus cell death (Lancaster et al. 2013). Obviously, the absence of a vascular system hampers the long-term survival and functioning of the ROs and thereby restricting the maturation and integration of the retinal cells. In ROs, RGCs are the first cell type to differentiate but are also the first cell type to die by necrosis. The human retina, during its *in vivo* development, is vascularized in situ both by choroidal capillaries and by an embryonic hyaloid artery. This is in significant contrast to the RO, where there is no vascularization and therefore limited diffusion of oxygen and nutrients from its outer layer to its innermost layer, where the RGCs are located. Although the recent use of a bioreactor can help the diffusion of nutrients and oxygen, it has not improved the survival of the RGCs in ROs (Distefano et al., 2018). It was observed by Wahle et al. (2023) that, in the ROs, the RGCs emerged at W6, became abundant at W12, and decreased till completely disappearing by W18. This was also in line with a known deficiency of ROs protocols, that is, progressive loss of RGCs in long-term culture as identified by Cowan et al. (2020) and Capowski et al. (2019). Moreover, the lack of projection targets in the free-floating environment also contributes to the RGC loss at later stages (Capowski et al., 2019; Wahlin et al., 2017; Zhong et al.,

2014). Therefore, the growth curve of RGCs has been the focus of only a few studies in ROs. It is thus very important and meaningful to provide a real-time curve of the initial growth and disappearance of RGCs in ROs, which hasn't been done before.

1.6 PiggyBac Transposon system

The PiggyBac system has two components: the transposase enzyme and the mobile genetic element, or transposon. Through its mechanism of action, transposase recognizes specific inverted terminal repeat sequences within the PiggyBac element. Thus, it excises the transposable elements of this system, which integrate at random into TTAA chromosomal sites distributed throughout the genome (Zhao et al., 2016) (Fig. 4). The production of the PiggyBac system is much safer and easier compared to viral vectors. It also has a larger packaging capacity ranging from 9.1 to 14.3 kilobases with higher levels of transposition activity in comparison with other transposons (Wilson et al., 2007). Thus, the PiggyBac system is one of the effective ways of inserting target genes into the stem cells and therefore can be used for the investigation of their properties. Synthetic promoters received from Jüttner et al. (2019) and fluorescent genes were introduced into 01F49i-N-B7 iPSCs as transgenes, herein abbreviated as B7 cells, and integrated into the genome of B7 cells.

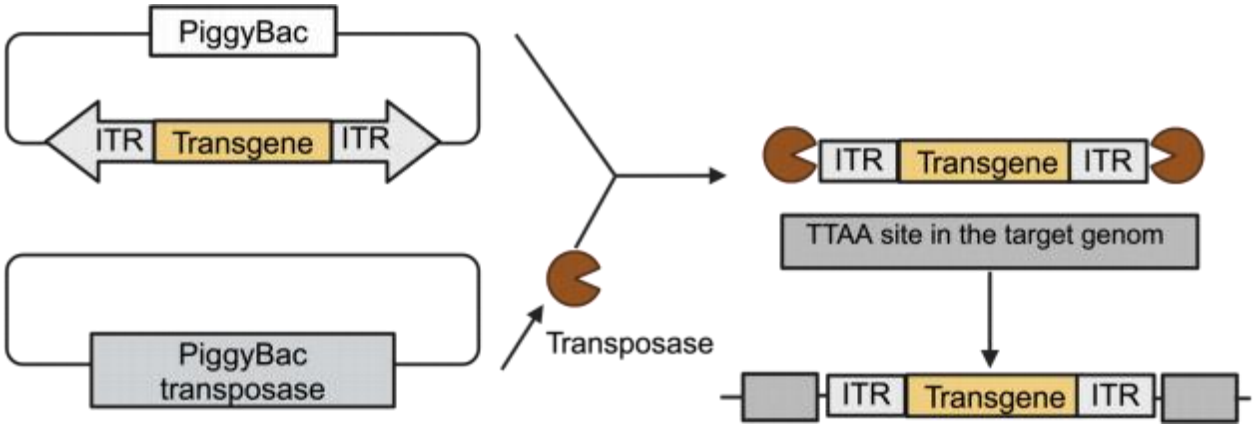

Fig. 4: Mechanism of the PiggyBac System: The PiggyBac system is composed of an expression cassette with a n transgene flanked at each end by an ITR. The enzyme transposase interacts with these ITRs and cleaves them, thus allowing for the expression cassette-transgene excision to integrate into a TTAA site within the host target genome. Images created at Biorender.com.

1.7 Fluorescent reporter genes and the integration into PiggyBac Transposon system

In general, reporter genes can be divided into two main groups: non-fluorescent proteins, which include lacZ, and fluorescent proteins, including green fluorescent protein. In this study, two fluorescent proteins, enhanced green fluorescent protein (EGFP) and tandem dimer tomato (tdTomato), were used to detect the emergence of the targeted retinal cells in real time via a fluorescence microscope. The green fluorescent protein (GFP) originally was isolated from the Victoria jellyfish by Shimomura et al. (1962). A breakthrough was achieved when Okabe et al. in 1997 used a variant of GFP, the EGFP, to produce the first green mouse (Okabe et al., 1997). EGFP is now used in a wide range of research. One of the challenges for the imaging systems is the ability to discriminate between two fluorescent proteins with similar spectra. To overcome this limitation, various colors and shades of fluorescent proteins were designed and synthesized. tdTomato is a unique color protein, higher in brightness, with a shorter maturation time that contributes to lower toxicity (Muzumdar et al., 2007). Plasmids in this study were designed to carry EGFP and tdTomato, which were downstream of the synthetic promoters D1 and A1 from the Roska laboratory, respectively (Jüttner et al., 2019) (Fig. 5). The synthetic promoter D1 is active in RGCs while A1 is in cones. After nucleofection, the plasmids were introduced into the nucleus of the B7 cell lines. The PiggyBac constructs also contained a ubiquitin c promoter (UBC), which is known to drive sTab., constitutive expression in a wide range of mammalian cell types (Schorpp et al., 1996). The UBC promoter drove the blasticidin and puromycin genes, allowing antibiotic selection of those nucleofected B7 cells with successfully integrated transgenes (Fig. 5). The cell lines of D1-EGFP and A1-tdTomato were used in the production of ROs. As soon as the synthetic promoters are activated, the downstream fluorescent genes will be expressed. Therefore, it enables a quick and real-time labeling of RGCs and cones. This provides a handy method to test the development of the retina along with cell type specification

rapidly, as cell differentiation and survival are crucial for the proper monitoring of retinal development.

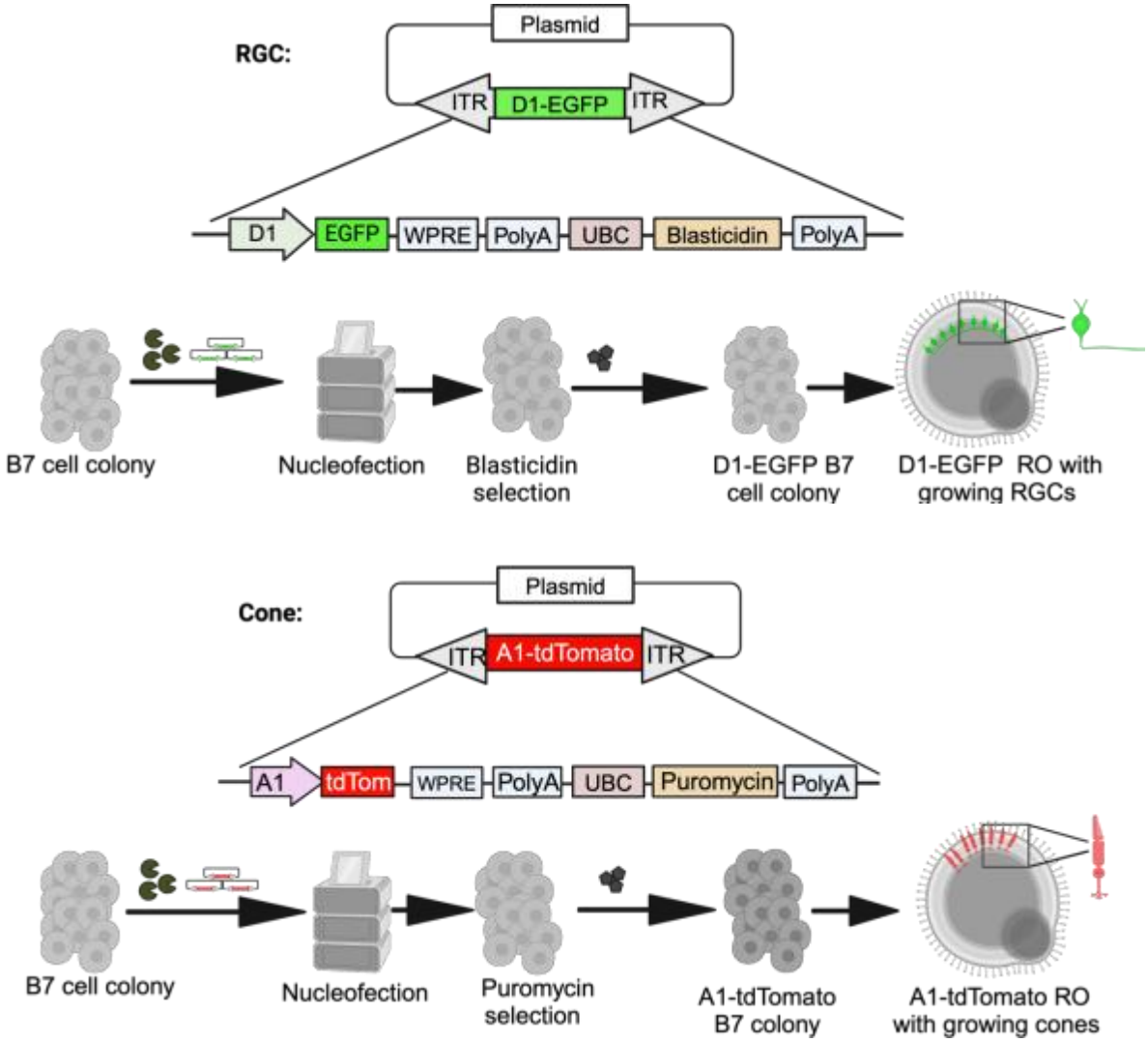

Fig. 5: PiggyBac constructs were nucleofected into B7 cell lines for targeting RGC and cone. EGFP was inserted downstream of the promoter D1 with a Blasticidin resistance gene as antibiotic selection marker, while tdTomato was inserted downstream of the promoter A1 with a puromycin resistance gene as antibiotic selection marker. RGCs derived from D1-EGFP ROs would show a green fluorescent signal and cones derived from A1- tdTomato ROs would show a red fluorescent signal. Images generated using Biorender.com.

1.8 Aim of this study

The main objective of this study is to label cones and RGCs using synthetic promoters. Since the emergence of retinal cells in ROs has not been previously documented in real time, this study provided a quick and convient way to detect the retinal cells, specifically RGCs and cones, using a fluorescence microscope (Fig. 6a). Using molecular cloning technique, namely Gibson assembly, two synthetic promoters are each linked to a downstream fluorescent gene. When the promoter is activated, the fluorescent signal is expressed and detected (Fig. 6a). In addition to live cell imaging, the identitiy of RGCs and cones was further confirmed by IHC (Fig. 6b). The identity of RGCs was additionally validated by FC and qRT-PCR (Fig. 6c and 6d).

Of note, the synthetic promoters A1 and D1 from the Roska lab have been characterized in mouse models and non-human primates, but have not been tested in the human ROs derived from the B7 stem cell line (Jüttner et al., 2019). This approach further confirms the functionality of these synthetic promoters in human B7 cell-derived ROs.

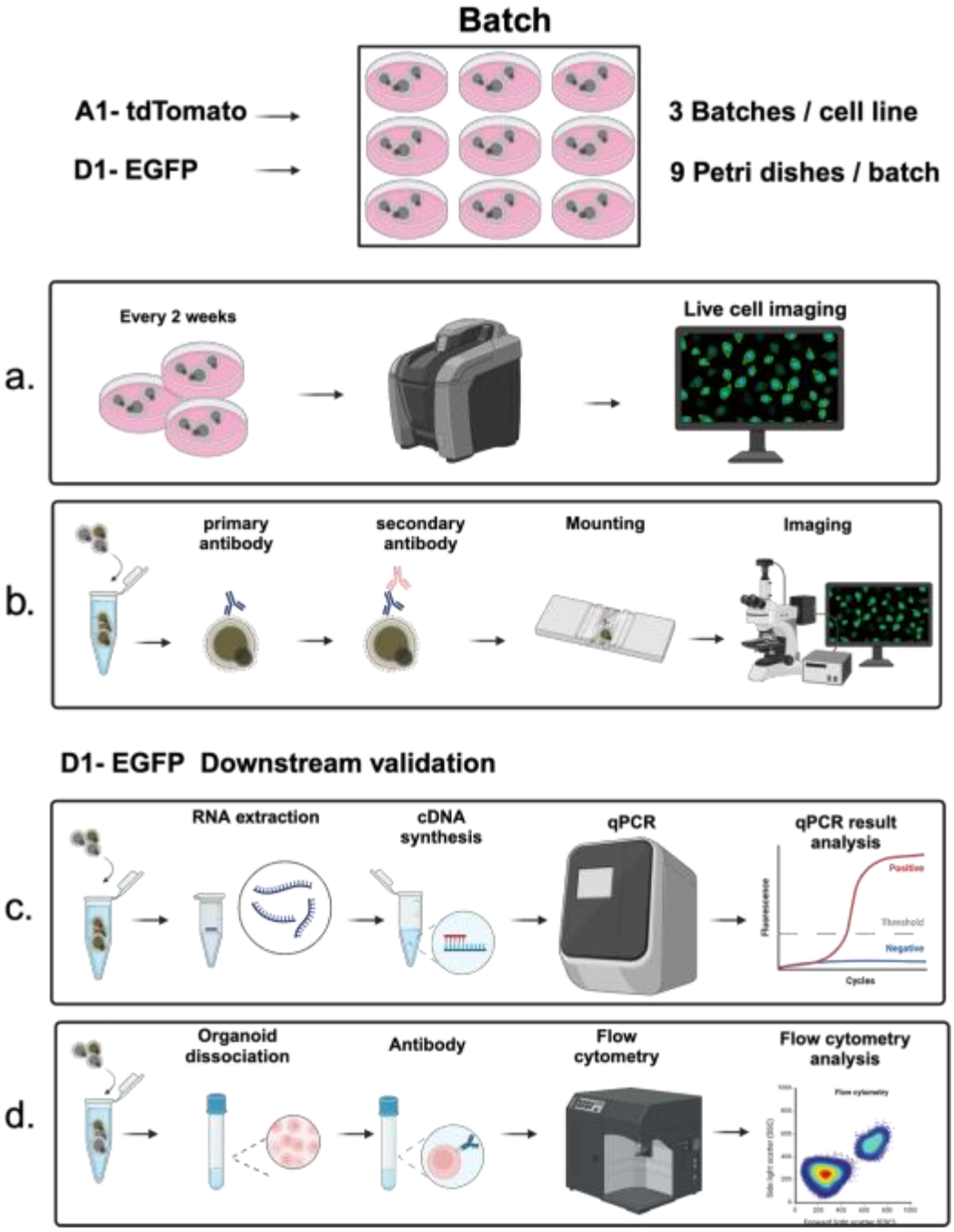

Fig. 6: Abbreviated schematic flow chart of ROs settings and analysis methods for RGCs and cones: Three independent batches composed of 9 Petri dishes per petri dish were prepared for each A1- tdTomato cell line and D1- EGFP cell line. Periodic live cell imaging of RGCs and cones development were achieved by using fluorescent microscopy (a). For IHC, ROs derived from A1- tdTomato cell line and D1- EGFP cell line were randomly periodically picked from batches and stained using mounting technique (b). In addition, ROs derived from D1- EGFP cell line were taken for further validation of RGCs by qRT-PCR (c) and flow cytometry (d). Images were generated using Biorender.com.

2. Materials and methods

2.1 Materials

Tab. 1: Lab equipment

Equipment	Source	Identifier
Eppendorf CryoCube -80°C	Eppendorf	JS5419090503
4D-Nucleofector Core Unit and X Unit	Lonza	20112821-1
Attune Nxt Acoustic Focusing Cytometer	Thermo Fisher Scientific	S2583255
CO2 Incubator	PHCbi	MCO-170M-PE
Countess II cell counter	Thermo Fisher Scientific	AMQAX1000
E-Gel Power Snap Electrophoresis System	Thermo Fisher Scientific	G8300
EVOS XL Core microscope	Thermo Fisher Scientific	AMEX1100
INCU-Line IL 23	VWR	3900482
ThermoMicer C	Eppendorf	2230000015
Nanodrop one Spectrophotometer	Thermo Fisher Scientific	ND-ONE-W
QIAcube	Qiagen	9002864
Quant Studio 3 Real Time PCR	Thermo Fisher Scientific	A29215
Visitron VisiScope Spinning Disk Microscope	Zeiss	CSU-X1
ProFlex PCR system	Thermo Fisher Scientific	4484075

Tab. 2 : Consumables, chemicals and enzymes

Name	Source	Identifier
2-Mercaptoethanol	Thermo Fisher Scientific	21985023
Accutase	Sigma	A6964-100ML
Agarose plates	Busskamp laboratory	
Blasticidine	Thermo Fisher Scientific	A1113903
Bovine serum Albumin (BSA)	Thermo Fisher Scientific	15260037

BsrGI-HF	New England Biolab	R3575S
B-27 Supplement without vitamin A	Thermo Fisher Scientific	12587-010
Carbenicillin	AppliChem	14046960
CloneAmp HiFi PCR Premix	Takara Bio	639298
CutSmart Buffer	New England Biolabs	B7204
D-glucose	MERCK	108337
DNase	Sigma	D4263
Dulbecco's Modified Eagle Medium (DMEM)	Thermo Fisher Scientific	10569-010
DMEM / F-12	Thermo Fisher Scientific	31331-028
Dulbecco's phosphate buffered saline (DPBS) without Ca^{2+} and Mg^{2}	Thermo Fisher Scientific	14190144
Dulbecco's phosphate buffered saline (DPBS) with Ca^{2+} and Mg^{2}	Thermo Fisher Scientific	14040133
Ethylenediaminetetraacetic acid (EDTA)	Thermo Fisher Scientific	15575020
E-GelTM EX 1 % Agarose	Thermo Fisher Scientific	G401001
Fetal bovine serum (FBS)	Thermo Fisher Scientific	16141002
Gibson Assembly Master Mix	New England Biolab	E2611S
GlutaMAX	Thermo Fisher Scientific	35050038
Heparin	Sigma	H3149-50KU
High-capacity cDNA Reverse Transcription kit	Thermo Fisher Scientific	4368814
KCL	MERCK	529552
L-cysteine	AppliChem	A3634
Matrigel	Corning	354234
$MgCl_2$-H_2O	MERCK	68475
MicroTissues 3D Petri Dish micro-mold spheroids	Sigma	Z764019-6EA
mTeSR	StemCell Technologies	85850

N2	Thermo Fisher Scientific	17502048
Na_2SO_4	MERCK	239313
NaCl	Sigma	S3014
NaH_2PO_4-$2H_2O$	MERCK	106342
$NaHCO_3$	MERCK	106329
Non-essential amino acids (NEAA) solution	Sigma	17502-048
Neurobasal A	Thermo Fisher Scientific	10888022
Normal donkey serum (NDS)	Sigma	S30-100ML
One Shot Stbl3	Thermo Fisher Scientific	C737303
Paraformaldehyde	VWR	J61899-AK
Papain	Worthington Biochemical	LS003127
Penicillin-Streptomycin	Thermo Fisher Scientific	15140122
Phosphate buffered saline (PBS)	Thermo Fisher Scientific	14190169
P3 Primary Cell 4D-Nucleofactore X kit	Lonza	V4XP-3024
PCR purification kit	Qiagen	28104
PowerUp SYBR Green PCR Master Mix	Thermo Fisher Scientific	A25741
Puromycin dihydrochloride	Thermo Fisher Scientific	A1113803
Qiagen Plasmid plus Midi Kit	Qiagen	12941
QIAprep Spin Miniprep kit	Qiagen	14035170
QIAquick Gel extraction Kit	Qiagen	14035180
ReLeSR	StemCell Technologies	100-0483
Retinoic acid	Sigma	R2625
RNeasy kit	Qiagen	74104
ROCK-inhibitor	StemCell Technologies	72304
SfiI	New England Biolabs	R0123S
S.O.C. medium	Thermo Fisher Scientific	15544034
Sodium azide	MERCK	08591-1ML-F
Sucrose	Sigma	S7903-250G

Taurine	Sigma	T0625-25G
Trypan Blue Solution	Sigma	14044188
TritonX100	MERCK	T9284-100ML
TrypLE	Thermo Fisher Scientific	12604013
Ultra-Pure H_2O	Thermo Fisher Scientific	10977035
X-VIVO	Lonza	881020

Tab. 3: Buffers and media

Name	Components
3:1 medium	75 ml DMEM with Glutamax + 25 ml F12 with Glutamax + 2 ml B27 without Vitamin A + 1 ml NEAA + 1 ml Pen Strep
3:1 N2 medium	70 ml DMEM with Glutamax + 20 ml F12 with Glutamax + 1 ml N2 Supplement + 1 ml NEAA + 1 ml Penicillin-Streptomycin + 10 ml ES FBS + 20 µl 500 mM Taurine
30 % Sucrose	30 g Sucrose + 100 ml DPBS without Ca^{2+} and Mg^{2+}
Activated papain solution	8U papain + 48 ul of "activator" for 30mins at room temperature (5 ml) + H_2O with 1.1 uM EDT A + 5.5 mM L-cysteine + 0.07 mM 2-mercaptoethanol + 950 ul ringer solution at 37 °C
Antibody solution	3 % NDS + 1 % BSA + 0.5 % Triton X- 100 + 0.02 % Sodium Azide
Blocking solution	10 % NDS + 1 % BSA + 0.5 % Triton X- 100
FACS buffer	0.2 ml 1 % FBS + 19.8 ml 1 mM EDTA
LB-Carbenicillin Agar-Plates	1 L LB medium + 15 g Agarose + 0.1 mg/mL Carbenicillin
Lysogeny Broth (LB) medium + Carb	5 g NaCl + 50 g Yeast extract + 10 g Tryptone + 0.1 mg/mL Carbenicillin in 1 L H_2O at pH 7.2
Neural induction media (NIM)	0.5 ml N2 Suupplement + DMEM/F12 1:1 with Glutamates + 0.5 ml NEAA + Heparin 2 ug/m
Ringer solution	125.6 mM NaCl + 1.2 mM $MgCl_2.H_2O$ + 3.6 mM KCl + 22.6 mM NaHCO3 + 21.7 uM $NaH_2PO_4.2H20$ + 1.2 mM Na_2SO_4 + 10 mM D-Glucose + 0.4 mM EDTA
Stop solution	49 ml Ice cold NeuroBasal A + 500 ul 2 mM Glutamax + 1 ml 2 % B27 supplement without Vit A + 33.3 ul 20 U/ml DNase

Tab. 4: Stains and antibodies

Antibody	Dilution	Clone	Source	Identifier
Anti-GFP mouse	1:200	GF28R, Monoclonal	Thermo Fisher Scientific	A11120
Anti-POU4F1 Rabbit	1:1000	Polyclonal	Synaptic system	411003
Anti-Recoverin Rabbit	1:1000	Polyclonal	Merck	AB5585-I
Donkey anti-mouse AF488	1:1000	A2120, Polyclonal	Thermo Fisher Scientific	A21202
Donkey anti-rabbit AF568	1:1000	A1004, Polyclonal	Thermo Fisher Scientific	A10042
Donkey-anti-rabbit AF488	1:1000	A2120, Polyclonal	Thermo Fisher Scientific	A21206
Hoechst	1:1000	H3570, polyclonal	Thermo Fischer	3570

Tab. 5: Plasmids and cell lines

Name	Function	Identifier
PB09-hSyn-ChRimson-YFP-UBC-puro	Backbone	IV-25 AG Busskamp
PB-mCAR-EGFP-BGH-UBC-Blasti	Backbone	IV-30 AG Busskamp
PB-ppl-mem-tdTomato-Blasti	Final Plasmid	IX-17 AG Busskamp
pAAV-ProA1-GCaMP6s	Promoter	Plasmid #126002 Addgene
pAAV-ProD1-GCaMP6s	Promoter	Plasmid #126005 Addgene
PiggBacTransposase	Encodes transposase for insertion of PiggyBac vectors	PB210PA-1-SBI
hiPSC line 01F49i-N-B7 (short name: B7)	University Hospital Basel ophthalmology	Cowan, Renner et al. 2020

Tab. 6: Primers

Name	Purpose	Source	Sequence
EGFP forward primer	PCR	Eurofins	TACGGGGAAAAGGCCTCCAC GGCCGCCACC

EGFP reverse primer	PCR	Eurofins	AGGATCCTCACTTGTACTTAT CACTTGTAC
TdTomato forward primer	PCR	Eurofins	TACGGGGAAAAGGCCTCCAC GGCCGCCACC
TdTomato reverse primer	PCR	Eurofins	TCCTCATTACTTTTACTTGTAC CATGGATC
ProA1 forward primer	PCR	Eurofins	ATACGGGGAAAAGGCCTCCA GAGGCAGGCC
ProA1tdtom reverse primer	PCR	Eurofins	ACAGCATGGTGGCGGCCGTT CTGCTGTCTC
ProD1 forward primer	PCR	Eurofins	ATACGGGGAAAAGGCCTCCA AGGTTTA
ProD1egfp reverse primer	PCR	Eurofins	GCTACACATGGTGGCGGCCG TGGCCTATAG
PiggyBac forward 485	Sequencing	Eurofins	CAAAACTTTTATGAGGGAC AG C
WPRE-Rev pLV 47	Sequencing	Eurofins	AAGCCATACGGGAAGCAATA
GFP forward primer	qPCR	Eurofins	CAACAGCCACAACGTCTATAT CATG
GFP reverse primer	qPCR	Eurofins	ATGTTGTGGCGGATCTTGAAG
POU4F1 forward primer	qPCR	IDT	CTCACTTTGCCATGCATCC
POU4F1 reverse primer	qPCR	IDT	AGCAGCGTCTCGTCCAG
SCL17A6 1 forward primer	qPCR	Eurofins	CCTCTACCCTAAATATGCTAA TTCCA
SCL17A6 2 reverse primer	qPCR	Eurofins	TTGCTCCATATCCCATGACAT
Beta-actin 1 forward primer	qPCR	Eurofins	ACAGAGCCTCGCCTTTG
Beta-actin 2 reverse primer	qPCR	Eurofins	CCTTGCACATGCCGGAG

Tab. 7: List of used Software

Name	Source	Identifier
Fiji	Microscopic image processing & analysis	https://imagej.net/software/fiji/
Graphpad Prism 9 v.9.0	Statistical analysis & Data Visualization	https://www.graphpad.com/
Microsoft Office	Data processing and writing	https://www.office.com/
Attune Nxt flow cytometer	Thermo Fisher Scientific	17192369
Benchling	In silico design of primers, vectors, and sequence alignments	https://www.benchling.com/
Biorender	Schematic design	https://www.Biorender.com/

2.2 Methods

2.2.1 Generation of PiggyBac constructs

Synthetic promoters A1 and D1 as well as fluorescent reporter genes EGFP and tdTomato were amplified with polymerase chain reaction (PCR). The summary of the PCR premix information, the brief standard PCR condition, and the forward and reverse primers used for the PCR are shown in Tab.s 8, .9, and 6, respectively. All the PCR primers were designed with great care by the Assembly Wizard function of the Benchling program. The reporter gene EGFP was amplified from the plasmid "mCAR-EGFP-BGH-UBC-Blasti" (AG Busskamp), whereas tdTomato was amplified from "pPB-plp-mem-tdTomato-Blasti" (AG Busskamp). Synthetic promoters were amplified from the plasmids supplied by Jüttner et al. (2019) (Tab. 5).

Tab. 8: Standard PCR premix for DNA-Amplification (Takara bio, ProFlex PCR Thermo Fisher Scientific)

Reagent	Volume	Final concentration
CloneAmp HiFi PCR Premix	12,5 µl	
10 µM forward primer	1.5 µl	0,3 µM
10 µM forward primer	1.5 µl	0,3 µM
Template DNA	<100 ng	
Sterilized water	Up to 25 µl	
Total volume per reaction	25 µl	

Tab. 9: Standard PCR condition for DNA-Amplification

Step	Temperature	Duration	Cycles
Initial denaturation	95 °C		1
Denaturation	98 °C	10s	30-35
Annealing	58 °C	5 sec	30-35
Extension	72 °C	5 sec/kb	30-35
Final extension	72 °C		1

5 µg of each PiggyBac plasmid referred to as backbone, PB-mCAR-EGFP-BGH-UBC-Blasti (AG Busskamp) and PB09-hSyn-ChRimson-YFP-UBC-puro (AG Busskamp), were separately digested firstly with 1 µl restriction enzyme BrsGI (New England Biolabs) and 5 µl CutSmart Buffer (New England Biolabs) at 37 °C for 1 hour and then with 1 µl SfiI (New England Biolabs) with 5 µl CutSmart Buffer at 50 °C for 1 hour. Along with the PCR products, the digested backbones were loaded into the 1 % Agarose E-Gel (Thermo Fisher Scientific), and then the electrophoresis was run on the E-Gel Power Snap Electrophoresis System (Thermo FisherScientific). Sample size was confirmed via a length ladder. DNA was then purified from the gel using a Qiagen Gel Extraction Kit (Qiagen). Concentrations of DNA were determined with a Nanodrop spectrophotometer (Thermo Fisher Scientific).To insert the reporter genes and synthetic promoters into the backbones, two successive GA reactions were performed with the fluorescent reporter gene first into the backbone, then the promoter (Fig. 7). The GA method allows for an easy assembly of more than two DNA fragments in one step by using a GA reaction mix composed of three enzymes (5' exonuclease,DNA polymerase, and DNA ligase) that

work together in a single isothermal reaction. DNA fragments of the GA were amplified using specific primers (Tab. 6). The overhang at the 5' end was designed to anneal with the adjacent DNA fragment for 15-20 base pairs, and the 3' end for a 15-20 base pair sequence, which anneals with the target DNA fragment (Fig. 8). The forward primers of fluorescent reporter genes for the study were designed with complementary sequences in order to add a restriction site for the enzyme SfiI, thereby allowing the insertion of the synthetic promoters in front. The DNA concentration was adjusted to each GA reaction that the total reaction volume was less than 10 µl. 10 µl of combined fragments from linearized backbone and fluorescent reporter gene were mixed with 10 µl of GA Master mix (New England Biolabs) and incubated at 50 °C for 45 minutes. Afterwards 1 µl SfiI with 5 µl CutSmart Buffer was mixed to 4 µl of the backone which is already incorporated with fluorescent reporter gene and incubated at 50 °C for 1 hour. These fragments from synthetic promoter and linearized backbone were then combined in a mixture with 10 µl of GA Master mix, incubated at 50 °C for 45 minutes to obtain the final backbone construct (Fig. 7).

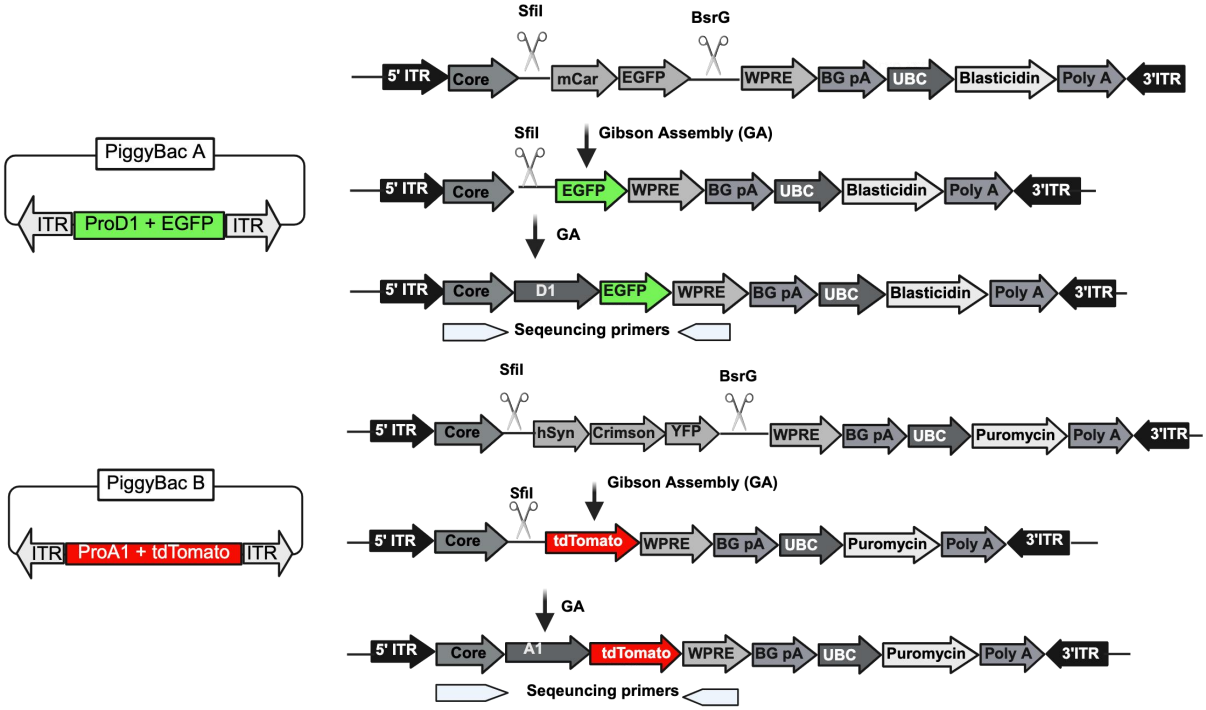

Fig. 7: Schematic overview of the molecular cloning strategy. The backbones were digested with SfiI and BsrGI enzymes. Fragments containing EGFP and tdTomato were obtained by PCR and integrated into the respective backbones using Gibson assembly. The backbones were linearized to allow the insertion of the synthetic promoters and fluorescent reporter genes. Images were generated using Biorender.com.

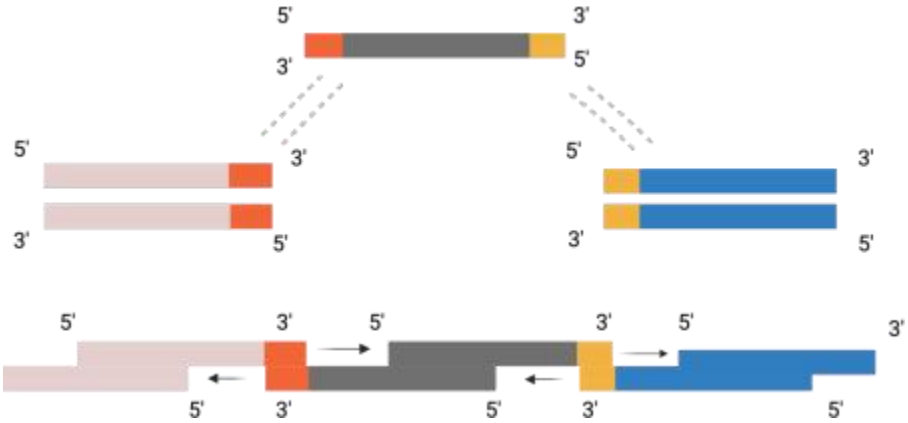

Fig. 8: The mechanism of Gibson assembly. Gibson assembly harnesses the collective action of three key enzymes in a single reaction: 5' exonucleases, the 3' extension activity of a DNA polymerase, and DNA ligase activity. Initially, the 5' exonuclease activity acts on the 5' ends of DNA fragments, cleaving them and exposing complementary sequences for annealing. DNA polymerase then elongates these fragments from the 3' to the 5' end, producing extended sequences. Finally, DNA ligase catalyses the joining of these elongated DNA fragments, resulting in a seamless and sTab. assembly. Images generated using Biorender.com.

4 µl of the final backbone product was added to the suspension of the One Shot Stbl3 chemically competent E. coli (Thermo Fisher Scientific), and the mixture was immediately heat shocked at 42 °C for 45 s, then returned on ice for 5 min to permit the bacteria to recover from thermal stress. To help the recovery process, 300 µl of SOC medium was added and then gently vortexed at 300 rpm. Incubation for 1 hour at room temperature was performed. After this incubation, the bacterial suspension was plated onto pre-warmed LB-Carbenicillin plates and were incubated overnight at 37 °C in the incubator. Colonies were randomly picked and subsequently analyzed by Sanger sequencing.

For sequencing, two primers were used: the forward primer being PiggyBac forward 485 and the reverse primer being WPRE-Rev pLV 47 (Tab. 6). The forward primer anneals into the center of the Core Insulator while the reverse primer anneals within the

Woodchuck Hepatitis Virus Posttranscriptional Response Element (WPRE) region (Fig. 7). According to the sequencing results, Positive colonies were selected and transferred into 50 ml flasks containing 50 ml of LB medium with the addition of 100 µl Carbenicillin (AppliChem). The bacteria were incubated overnight at 37 °C with shaking at 180 rpm for 16 hours. Then, on the following day, the bacterial culture was transferred to 50 ml tubes and centrifuged at 6000 g for 15 min at 4 °C. DNA was extracted from the bacterial pellets using the Qiagen Midi prep kit. The concentrations of the extracted DNA were measured via Nanodrop and the plasmids were stored at 20 °C.

2.2.2 Cell culture of iPSC line and nucleofection of PiggyBac constructs into iPSC line

The following study is based on the use of the iPSC line 01F49i-N-B7, henceforth referred to as the B7 cell line, which was via Transfer Agreement obtained from IOB, Switzerland. Maintenance: B7 cells were cultured in 6-well plates in pre-coated Matrigel (Corning). To expand B7 colonies, TrypLE (Thermo Fisher Scientific) was added to dissociate colonies into single cells for 5 minutes. For cell passaging, 100,000 cells per well were seeded and 10 uM Rock inhibitor (StemCell Technologies) was added for supporting the recovery of single cells after passaging. It was grown to about 80 % confluency and detached using TrypLE again. Cells were re-suspended in mTeSR (StemCell Technologies)and subsequently counted for nucleofection.

Nucleofection, also known as electroporation, is a physical transfection method that uses specific reagents and an electrical pulse to permeabilize the cell membrane to introduce DNA, RNA, or protein molecules into target cells. Here, nucleofection was performed using the Lonza 4D nucleofector system (Lonza). Each PiggyBac construct has its corresponding killing control for antibiotic selection after nucleofection (Tab. 13). The protocol of material preparation is summarized below (Tab. 12).

Tab. 10: Condition for Nucleofection

Reagent	Volume
DNA for Transaction	10 µg
P3 Solution	82 µl

Supplement	18 µl
PiggyBac Transposon	1/4 amount of the selected construct
IPS cells amount	800 000

Tab. 11: Construct design and Killing controls.

Name	Cell line
Cones only red puromycin	A1-tdTomato cell line
Ganglion cells only green blasticidin	D1-EGFP cell line
Killing control blasticidin	B7 cell line
Killing control puromycin	B7 cell line

10 µl of cell suspension from dissociated B7 cells was mixed with 10 µl of trypan blue (Sigma). Only dead cells can be stained by trypan blue through the porous cell membrane into the cytoplasm. Next, 800,000 cells were transferred to a new 2 mL tube and again spun at 100 x g for 3 min. The media supernatant was aspirated, and the cell pellet was re-suspended in the 100 µL P3 supplement mix containing 82 µL nucleofection solution and 18 µL supplement solution (Lonza). The cell suspension was then gently mixed with the prepared 10 µg PiggyBac constructs and 2.5 µg PiggyBac transposon (III-25). The solution was then gently mixed, transferred to a cuvette and placed in the Lonza Nucleofector, which nucleofected the cells with the CB-156 pulse. The coated 6-well plates were washed with DPBS medium containing Ca^{2+} and Mg^{2+} (Thermo Fisher Scientific) and then loaded with pre-warmed 1 mL mTeSR medium containing 10 uM Rock inhibitor. The suspension of nucleofected cells was mixed with the prepared media in the plates. The plates were then incubated at 37 °C. 24 hours after nucleofection, antibiotic selection was started in mTeSR medium containing 10 uM Rock inhibitor. After 48 h, the medium was changed to fresh mTeSR with antibiotic. Specifically, 4 µl of 10 mg / ml blasticidin (Thermo Fisher Scientific) and 0.6 µl of 10 mg / ml puromycin (Thermo Fisher Scientific) were required per 2 µl per well in the corresponding group (Tab. 12). Selection was continued until all cells in the killing controls were dead.

2.2.3 Generation of retinal organoids

The generation of retinal organoids (ROs) was based on the AMASS protocol by C.S. Cowan et al. (2020) (Fig. 9). The RO generation using the nucleofected cells from this project was mainly done by Kritika Sharma (PhD student) and maintenance was performed by the undergraduate students Richa Joshi and Karla Vollmerig. The 9 x 9 Agarose microwell arrays (each microwell array mold contains 81 microwells) were formed using MicroTissues 3D Petri Dish micromould spheroid moulds (Sigma). Agarose microwell arrays were prepared from 2 % agarose (Thermo Fisher Scientific) dissolved in 500 µl DMEM with GlutaMax (Thermo Fisher Scientific). The solidified moulds were transferred to 12-well plates (Corning) after sterilization under UV-light and equilibrated with 1.5 ml of mTesR medium (StemCell Technologies). Before use, the moulds were warmed in an incubator at 37 °C. 600 B7 cells were calculated per microwell. The B7 cells in wells were washed with 1 mL PBS twice (Thermo Fisher Scientific) and incubated for 5 minutes with 600 µl of 0.5 mM EDTA (Thermo Fisher Scientific) working solution at 37 °C. The EDTA was aspirated and 500 µl of Accutase (Thermo Fisher Scientific) was added and the plates were incubated at 37 °C for 3 minutes. 1 ml mTesR medium was added each well and the cells were gently pipetted up and down to generate a single cell suspension for cell counting. 5 ml of mTesR medium was added and the cell suspension was transferred to a 1.5 ml reaction tube and spun down at 200 g for 5 minutes. The supernatant was removed, and the cells were re-suspended in 150 µl of mTeSR medium containing 10 uM Rock-inhibitor. 150 µl of cell suspension was then added into the top of the agarose mold and allowed to settle at 37 °C. After a 30-minute incubation, 1.5 ml of mTesR medium + ROCKi 10 uM was added to completely cover the agarose mould and the forming EBs were incubated at 37 °C. The medium was replaced with 1/3 neural induction media (NIM) on day 1, then 1/2 NIM on day 2, and all medium was replaced with NIM on day 3. From day 3 to day 15, the RO dishes were supplemented with 2 ml of NIM, with the medium changed every 2 days. On day 7, EBs were transferred to a 6-well plate

coated with Matrigel. On day 15, the NIM medium was replaced with 3:1 medium (Tab. 3). On day 28, a checkerboard scraping technique was used to break the tissue sheets into smaller pieces. Cell debris and individual cells were washed 3 times with 3:1 medium. From day 42, the medium was changed to 3:1 medium with the addition of 100 µM taurine (Sigma) and 10 % FBS (Thermo Fisher Scientific). The medium was changed every other day. From week 10, the medium was supplemented with 1 µM retinoic acid (Sigma). From week 14, the medium was replaced with 3:1 N2 medium (Tab. 3).

Fig. 9: Timeline of RO generation with media change over time in abbreviated depiction. Image was generated using Biorender.com.

2.2.4 ROs tissue dissociation and flow cytometry

The randomly collected ROs underwent washes twice with 1 ml of ringer solution to maintain their osmolarity and morphology. Subsequently, 300 µl of activated papain solution (Worthington Biochemical) was added to each tube which was then incubated at room temperature for 35 minutes. Afterward, the tubes were placed on ice, and 1 ml of stop solution (Tab. 3) was added. The samples were centrifuged at 200 g at 4 °C for 30 seconds. The supernatant was gently removed, and the samples were washed with 1 ml of stop solution before being centrifuged again. Next, 300 µl of organoid dissociation solution was added to each tube, and the ROs were triturated with a 1 ml tip to achieve complete dissociation. The tubes were centrifuged once more at 300 g at 4 °C for 30 seconds. The cells were collected and re-suspended in 1 ml of DPBS (Thermo Fisher Scientific) containing 0.04 % BSA (Thermo Fisher Scientific). Then, the samples were centrifuged at 1400 g for 4 minutes, the supernatant was discarded, and the pellets were re-suspended evenly in 100 µl of FACs buffer (Tab. 3). Subsequently, 5 ml of DPBS medium without Ca^{2+} Mg^{2+} was added per tube and centrifuged at 1400 g for 4 minutes. The supernatant was carefully removed, and the

pellets were re-suspended in 1 ml of FACS buffer (Tab. 3). Finally, the flow cytometer (Thermo Fisher Scientific) conducted the analysis.

2.2.5 RNA Isolation, cDNA synthesis and RT-qPCR

To analyze the generated ROs on a transcriptomic level, qPCR was performed. First, ROs were packed into prepared 2 ml tubes to harvest RNA for qRT-PCR analysis. The RNA was further mixed well with the addition of 300 µl of RLT buffer (Qiagen), incubated at -20 °C for 2 hrs. The samples were processed using the QIAgenCube (Qiagen) and RNA Isolation solutions from QIAgen RNAasy Mini Kit (Qiagen). Isolation of RNA was followed by immediately placing the samples on ice. The concentration of RNA was determined by a Nanodrop (Thermo Fisher Scientific) to calculate the required volume in later cDNA transcription. The cDNA Reverse Transcription Kits (Thermo Fisher Scientific), were used for reverse transcription of the isolated RNA into cDNA. 1 µg RNA per reaction was required. The volume of each RNA sample had to be calculated based on the concentration. For low concentrations, 14.2 µl volume was taken. Then, the High-capacity cDNA Reverse Transcription Kit Master mix (Thermo Fisher Scientific) was equally distributed into each reaction tube placed on ice and gently mixed before addition. The reaction was performed using the ProFlex PCR system (Thermo Fisher Scientific). After reverse transcription, the cDNA concentration was measured again using the Nanodrop (Thermo Fisher Scientific). Thereafter, 10 ng of cDNA was calculated per sample and 10 µl PowerUP SYBR Green Mix (Thermo Fisher Scientific) for qRT-PCR was prepared for each reaction. Primers used for qRT-PCR are listed in Tab. 2.6 and abbreviated protocols are given in Tab.s 2.12 and 2.13.

For qRT-PCR analysis, the relative fold change expression compared to the chosen control group were calculated by ΔCt method. For each sample, ΔCt [sample gene] = Ct [sample gene] – sample Ct [housekeeping gene]. For experimental group: ΔΔCt [sample gene experiment] = ΔCt [sample gene experiment] – average ΔCt [control].Therefore, the relative fold change expression= $2^{-\Delta\Delta Cq}$.

Tab. 12: cDNA reaction mix and cycler program (High-capacity cDNA Reverse Transcription Kit, Thermo Fisher Scientific)

Reagent	Volume	Time	Temperature
10x RT Buffer	2 µl	10	25
25xdNTP Mix (100mM)	0,8 µl	120	37
10x Random Primers	2 µl	5	85
Reverse Transcriptase	0,5 µl	∞	4
RNA in Nuclease-free water	1 µg		
Nuclease-free water	To 19,5 µl		

Tab.13: Abbreviated qRT-PCR reaction mix and cycler program (PowerUP SYBR Green Mix, Thermo Fisher Scientific)

Reagent	Volume	Time	Temperature
PowerUp SYBR Mix	10 µl	2 min	50
Forward primer	1 µl	10 min	95
Reverse primer	1 µl		
cDNA	10 ng	15 s	95 40 cycles
dH_2O	Up to 20 µl	1 min	60
Volume in total	20 µl		

2.2.6 Immunohistochemistry staining

Day1: 6 ROs were chosen for respective constructs and put on a pre-prepared 12-well plate. 4 % of PFA (Thermo Fisher Scientific) used for fixing covered all ROs for 15 min at RT. Subsequently, PFA was removed, and the wells were washed 2 times with DPBS medium without Ca^{2+} Mg^{2+} (Thermo Fisher Scientific). Then 1 ml DPBS medium without Ca^{2+} Mg^{2+} was added per well for washing overnight at 4 °C.

Day2: PBS (Thermo Fisher Scientific) was changed to 30 % sucrose solution (Sigma) to decrease the cell damage during freezing 30 g sucrose (Sigma) dissolved in 100ml DPBS medium without Ca^{2+} Mg^{2+}. The ROs were incubated in sucrose solution (Tab. 3) overnight at room temperature.

Day3: The freeze (5 min) and thaw cycles (10-15 mins) were repeated for 5 times using freezing blocks and dry ice to permeabilize the cell membranes. The blocking solution (Tab. 3) was added and incubated at room temperature for 1 h. Subsequently, the primary antibodies Anti-GFP mouse (Thermo Fisher Scientific), Anti-Recoverin Rabbit

(Thermo Fisher Scientific) and anti- POU4F1 Rabbit (Synaptic system) were given in antibody solution and incubated at room temperature for 4 days.

Day7: The secondary antibodies Anti-mouse AF488 (Thermo Fisher Scientific) binding on Anti-GFP mouse, Anti-rabbit AF568(Thermo Fisher Scientific) binding on Anti-POU4F1 Rabbit, Anti-rabbit AF488(Thermo Fisher Scientific) binding on Anti-Recoverin Rabbit (Thermo Fisher Scientific), Hoescht (Thermo Fisher Scientific) binding on dsDNA in cell nucleus were added. All the secondary antibodies were prepared in 1:1000 dilution in antibody solution. Blocking solution, 30 % sucrose solution and Antibody solution were pre-prepared see in Tab. 3.

2.2.7 Statistical analysis

Graphpad Prism 9 and Excel were used to analyze collected data from qRT-PCR and FC. Statistical tests were chosen in terms of the type of data and the normality. The p-values and the types of statistical tests were labeled in each Figure.

3. Results

3.1 Validation of the plasmids and subsequent nucleofection in B7 cell lines

Colonies of the Stbl3 bacteria transfected with PiggyBac constructs were randomly picked for DNA sequencing. The results of sequencing were obtained as digital files from Microsynth. Correct overlap in the plasmid was corroborated using alignment-analysis from Benchling. Positive colonies of the Stbl3 bacteria, referred to as those that showed correct overlap in the analysis were picked for further plasmid DNA harvesting. The plasmids were then nucleofected into B7 cells for RO generation. Selection of nucleofected B7 cells stably expressing the transgene was performed using puromycin and blasticidin. Successful selection required a minimum of two days for puromycin-resistant cells and a minimum of five days for blasticidin-resistant cells. The free-floating dead cells all over the plates in the killing controls signified the successful antibiotic selection. In this study, 5 days were required for puromycin selection and 7 days for blasticidin selection in each killing control. The B7 cells that successfully took up the nucleofected transgenes in experimental groups grew healthily and confluently after selection (Fig. 10).

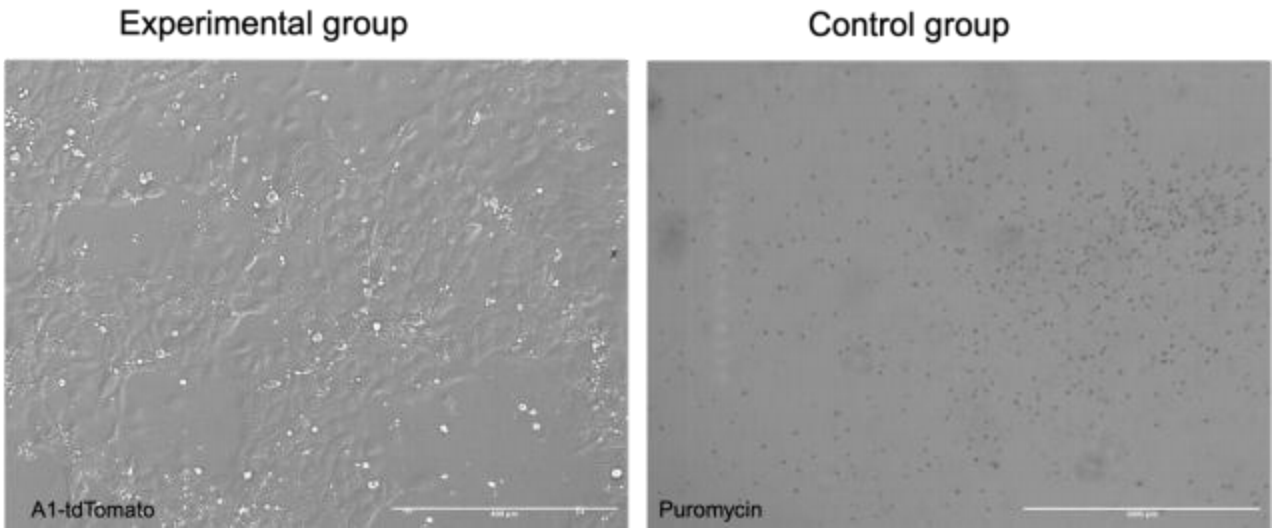

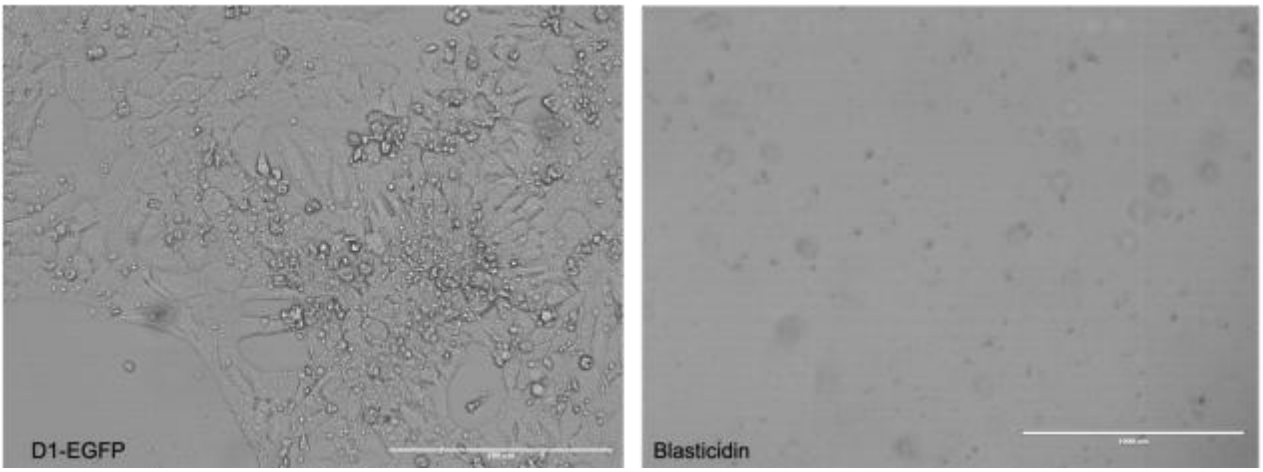

Fig. 10: The antibiotic selection after nucleofection. The left column displays the results of antibiotic selection of the experimental groups: the upper panel shows A1-tdTomato-expressing B7 cells after 5 days of puromycin selection, while the lower panel presents D1-EGFP-expressing B7 cells following 7 days of blasticidin selection (magnification: 20x; scale bar: 400 µm). The right column represents the killing controls. Non-nucleofected B7 cells subjected to puromycin treatment exhibited complete cell death after 5 days, characterized by the presence of floating cells debris as observed under light microscopy. In contrast, cells treated with blasticidin underwent cell death after 7 days (magnification: 10x; scale bar: 1000 µm. Images were generated using Fiji software and Biorender.com.

3.2 Live-cell imaging within ROs using fluorescence microscopy

Fluorescent microscopy images were taken regularly from ROs to document and observe the differentiation stages of RGCs and cones (Fig. 11). In the case of RGCs, no EGFP signal was detected within the first six weeks, and initial signals appeared at W7. At W7 and W8, some ROs showed a moderate expression of EGFP with some dendrite-like or axon-like projections (Fig. 11a). From W9 to W11, there was a relative increase compared to the previous stages in the number of RGCs expressing EGFP, with an increased number of RGCs displaying axon-like projections of variable length and amount (Fig. 11b). W12 showed an obviously high density of fluorescent RGCs overall compared to earlier stages. W14 showed more RGCs with long, extending axons, while the overall density of fluorescent RGCs decreased (Fig. 11).

The first appearance of cones was discernible at W14, with signals becoming more sharpened and almost exclusively localized in the outer margin of the ONL. To note, not

every RO and not every region within GCL or in ONL of fluorescence expressing ROs exhibited fluorescent signal consistently during the whole 14 weeks (Fig.11a).

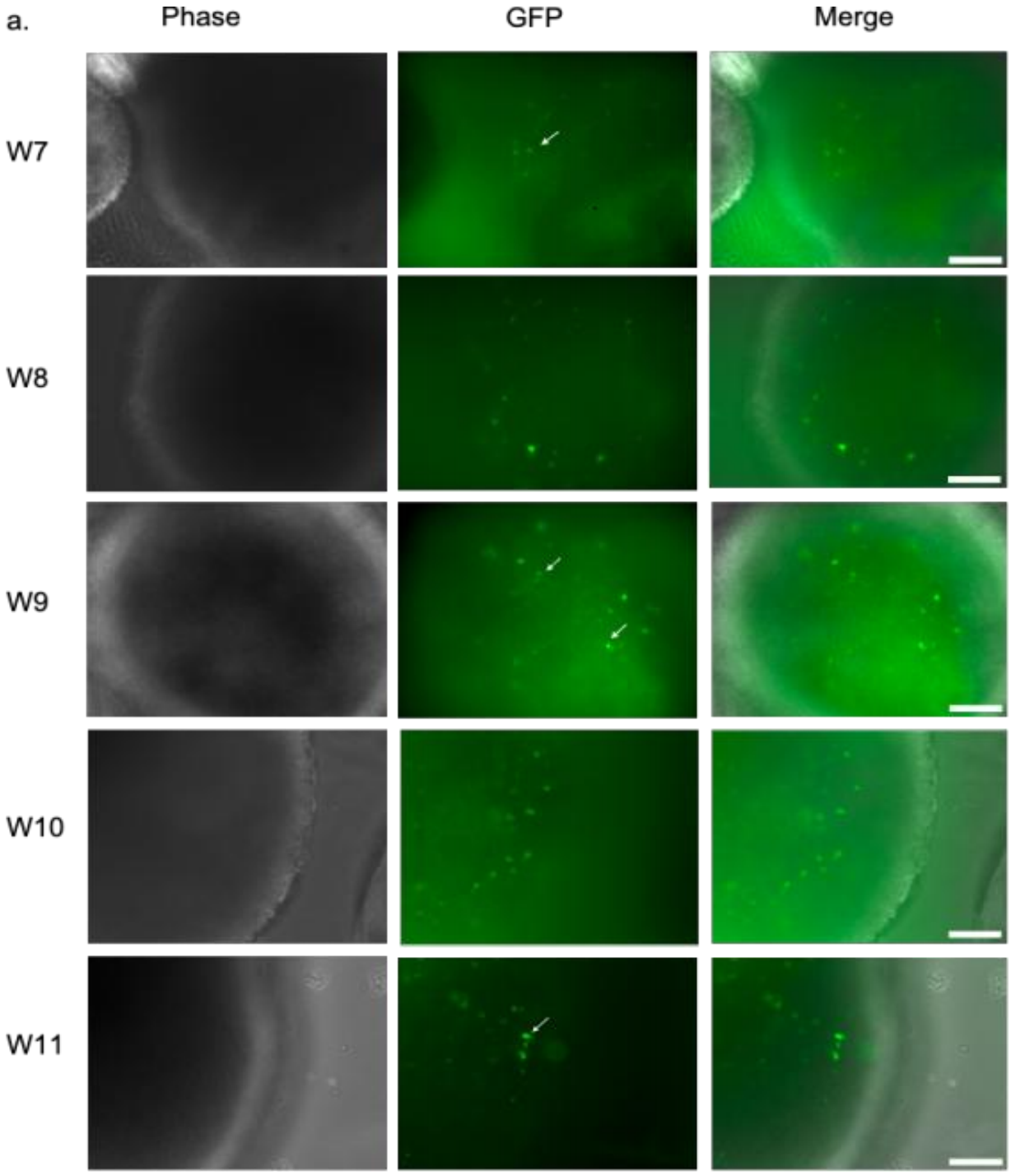

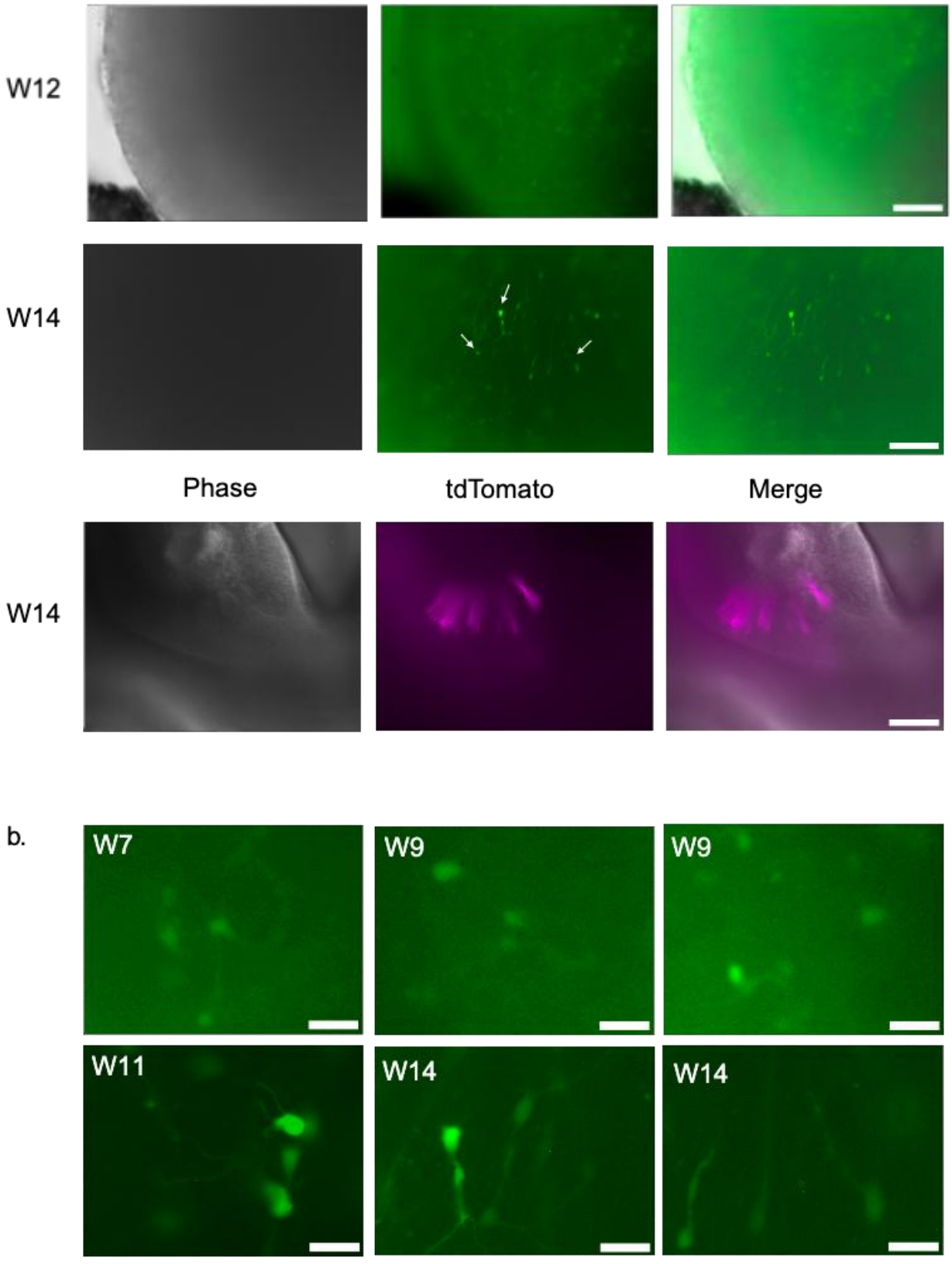
W12
W14
Phase
tdTomato
Merge
W14
b.
W7
W9
W9
W11
W14
W14

Fig. 11: Live-cell imaging of D1-EGFP ROs and A1-tdTomato ROs. a) Visualization of GFP-expressing RGCs and tdTomato-expressing cones under fluorescent microscopy at 20x magnification; Scale bar = 100 µm. b) Zoomed in images from various differentiation stages of RGCs at different time points, characterized by extending axons and dendrites; Scale bar = 50 µm. Images were generated using Fiji software and Biorender.com.

3.3 RGCs and cones targeting in ROs *in vitro*

IHC was used to validate the labeled cell types at various stages of differentiation. Cones, derived from A1-tdTomato ROs, were stained by anti-Recoverin, while RGCs derived from D1-EGFP ROs were stained by anti-POU4F1. The red fluorescent protein wasnot stained but were directly visualized using their respective fluorescence channels (channel 568 for tdTomato). The GFP fluorescent protein was stained by anti-GFP. Additionally, Hoechst was used to stain cell nuclei. In the anti-POU4F1- staining, where the nuclei were predominantly stained, numerous cells exhibited either GFP+ or POU4F1+ signals, but only a small subset of RGCs showed co-labeling of GFP and the RGC-specific marker anti-POU4F1 (Fig. 12). In summary, the majority of RGCs displayed separate signals than globally coincident signals.

The anti-Recoverin antibody stained primarily the cytoplasm of PRs. By W13, the majority of cones were successfully stained with anti-Recoverin antibody, which coincided with a strong tdTomato signal (Fig. 13). However, tdTomato presented a more pronounced signal in both the IS and OS of the cones, whereas anti-Recoverin mainly stained the OS (Fig. 13).

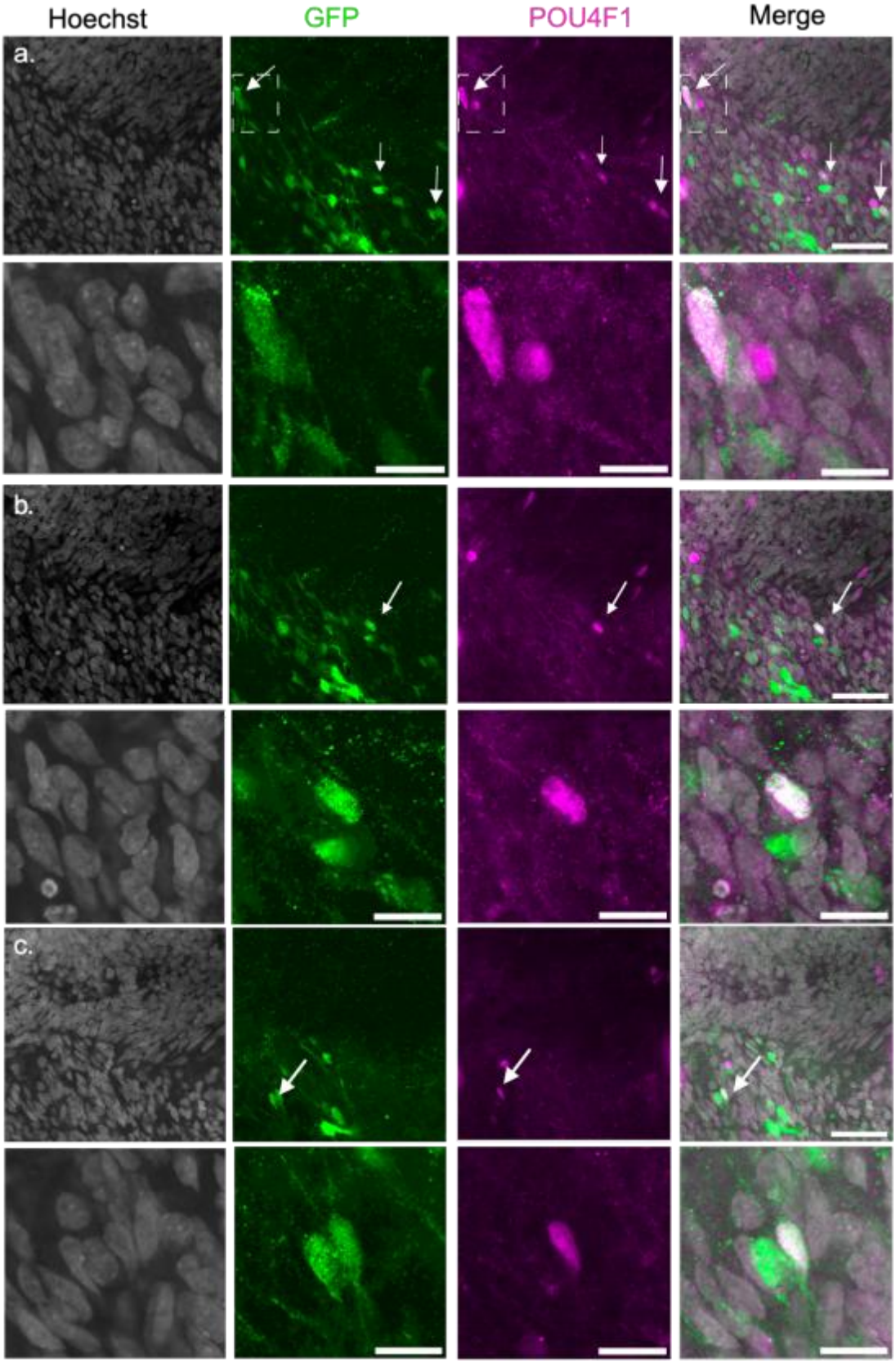

Fig. 12: IHC for RGCs in ROs at W13. Depiction: Confocal images of RGCs at W13: left Hoechst in channel 405(gray), middle left GFP in channel 488 (green) middle right

POU4F1 in channel 568 (magenta), right merge depiction of GFP and POU4F1 and nuclear stain; Scale bar = 50 µm. Zoomed-in images of the region boxed with dotted line are displayed below each slide; Scale bar = 15 µm. Images were generated using Fiji software and Biorender.com.

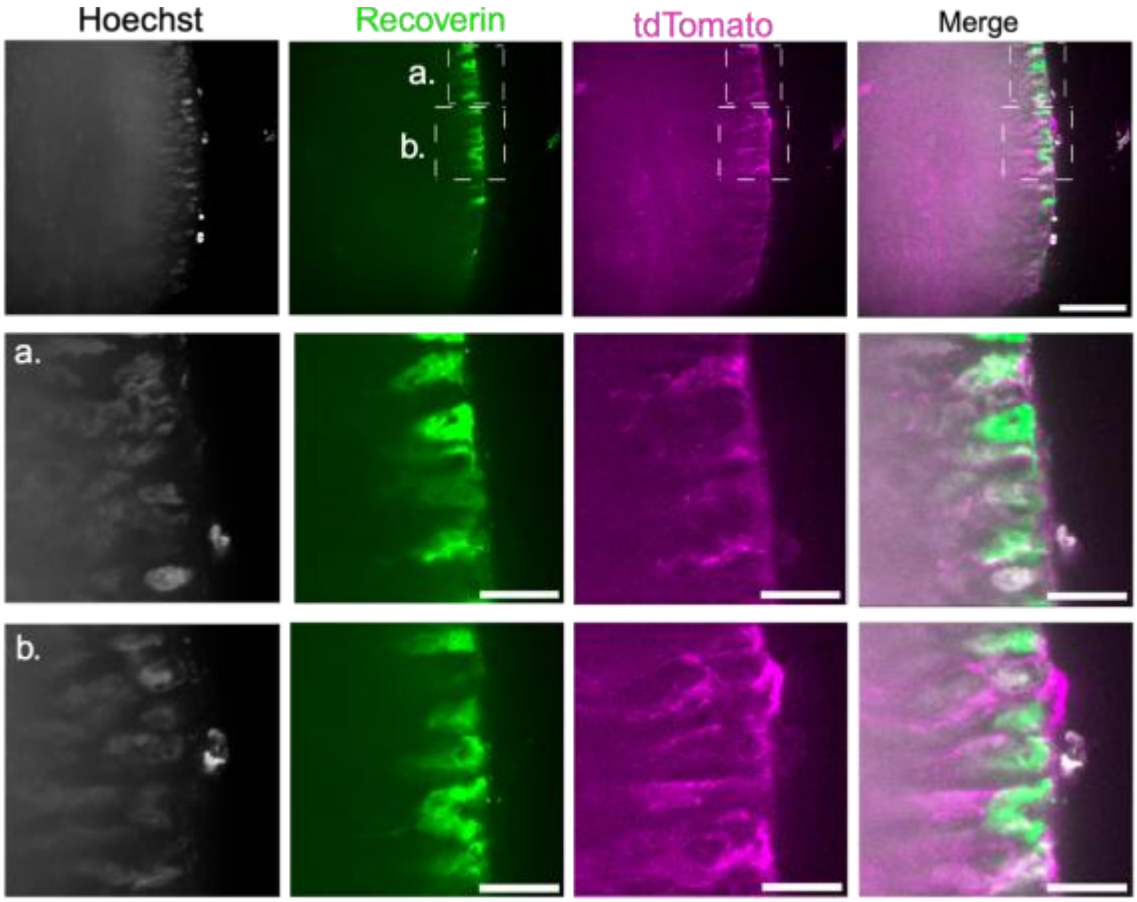

Fig. 13: IHC for cones in ROs at W13. Depiction: Confocal images of cones at W13: left Hoechst in channel 405(gray), middle left Recoverin in channel 488 (green) middle right tdTomato in channel 568 (magenta), right merge depiction of tdTomato and Recoverin and nuclear stain; Scale bar = 50 µm. Zoomed in images of the region a. and b. boxed with dotted line are shown below; Scale bar = 15 µm. Images were generated using Fiji software and Biorender.com.

3.4 Flow cytometry analysis of RGCs

FC analysis quantified the percentage of positive GFP-labelled live cells, which are RGCs. A histogram is presented to illustrate levels of GFP expression in the D1-EGFP group compared to the control group at different time points (Fig. 14). The control group refers to ROs that were generated from the original B7 cell lines without nucleofection. A 2-way ANOVA was used for analysis. The histogram represents the values of the samples,

expressing GFP expression over time (Fig. 14). The tendency for an increase in the percentage of GFP+ cells was progressively observed in the D1-EGFP group from W6 to W12, although there was a slight overall decrease at week 8. Some samples in the D1-EGFP group showed GFP expression exceeding 30 % both at W10 and W12, while at other time points their expression remained below 10 %. In addition, a small number of cells in the control group exhibited weak background autofluorescence at week 14. The p-value was not statistically significant between two groups or between data from one group at different time points throughout this study (Fig. 14).

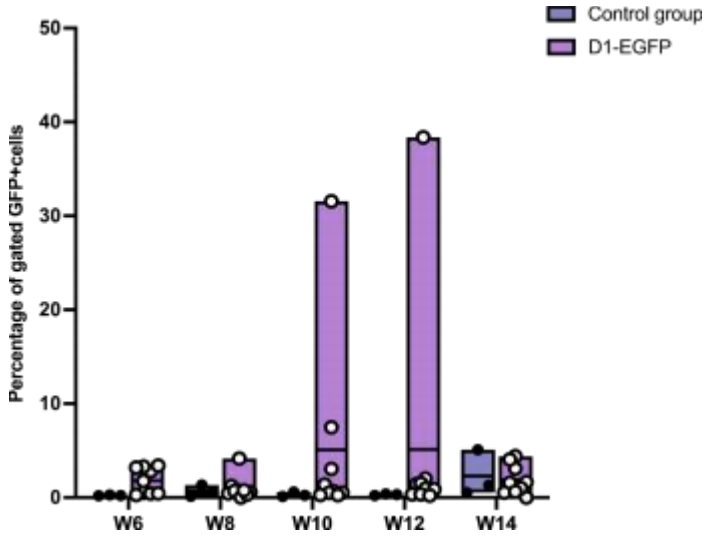

Fig. 14: Representative flow cytometry results depict the GFP+ cells in ROs at different time points. ROs were stochastically picked every 2 weeks. The percentage of gated GFP+ cells, defined as RGCs successfully derived by synthetic promoters, is depicted. The control group refers to ROs generated from the B7 cell lines without nucleofection. N=3, n=3 for control group; N=9, n=3 for D1-EGFP group, 2-way ANOVA test was performed, p value is insignificant. Image was generated using Graphpad Prism. .

3.5 Gene expression profile of RGCs

In this study, qRT-PCR was used to analyze the gene expression profiles of the RGCs as an extra downstream analysis. In this experiment, in addition to the GFP gene expression level, the expression level of *SCL17A6* and *POU4F1*, which are expressed by RGCs, were also analyzed. For exhibiting GFP expression in D1-EGFP group over time, all data were normalized to the data in D1-EGFP at W6. A histogram was thus generated showing the individual sample values. For the expression of the SCL17A6 and POU4F1 genes, a violin box graphic has been created respectively (Fig. 16). The experimental

group was termed D1- EGFP, and the control group, as mentioned above, refers to ROs generated from the original B7 cell lines without nucleofection. qRT-PCR data for *POU4F1* and *SCL17A6* expression were normalized to the control group at W6 to compare possible differences in RGC differentiation between the experimental and control groups. No outliers were excluded due to the small sample size (Fig. 16).

The histogram presented in Fig. 3.5 shows an increment of GFP expression level from W6 to W10 and then an apparent dip at W12. Taken together, it represented an upward trend of expression over time, and W10 and W14 showed especially high increases. However, many of the samples at week 12 showed unexpectedly low GFP expression, which may be attributed to technical variability or measurement errors introduced during manual handling. Therefore, the data from week 12 should be interpreted with caution and are not suiTab. for direct statistical comparison with other time points.

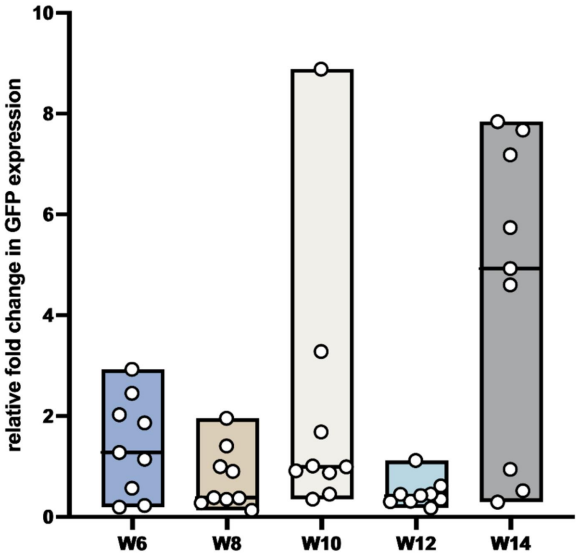

Fig. 15: The relative fold change in GFP expression in D1-EGFP ROs at different time points. All data were normalized to the D1-EGFP at W6. Data was represented as Min to Max with median. N=9, n=3 for D1-EGFP. Due to the inaccuracy of the data in week 12, ANOVA t-test cannot be performed. Image was generated using Graphpad Prism 9.

In Fig. 3.6A, it exhibited no significant differences in *SCL17A6* expression between the control and D1-EGFP groups. Some samples of D1-EGFP exhibited 3-4-fold changes at W6, W10, and W14, while all control samples were less than 2-fold during the experiment (Fig. 16A). Similarly, no significance was observed between the control group and the

D1-EGFP group in *POU4F1* expression as well (Fig. 16B). While the expression of *POU4F1* in the D1-EGFP group increased gradually along with time, the expression in a few samples was low. In the control group, one sample showed a 4-fold change at W6 and W8 that then diminished to levels constantly below a 2-fold change (Fig. 16B).

Taken together, the *SCL17A6* and *POU4F1* expression levels in both the wild type and D1-EGFP were not significantly different, and gene expression varied among samples.

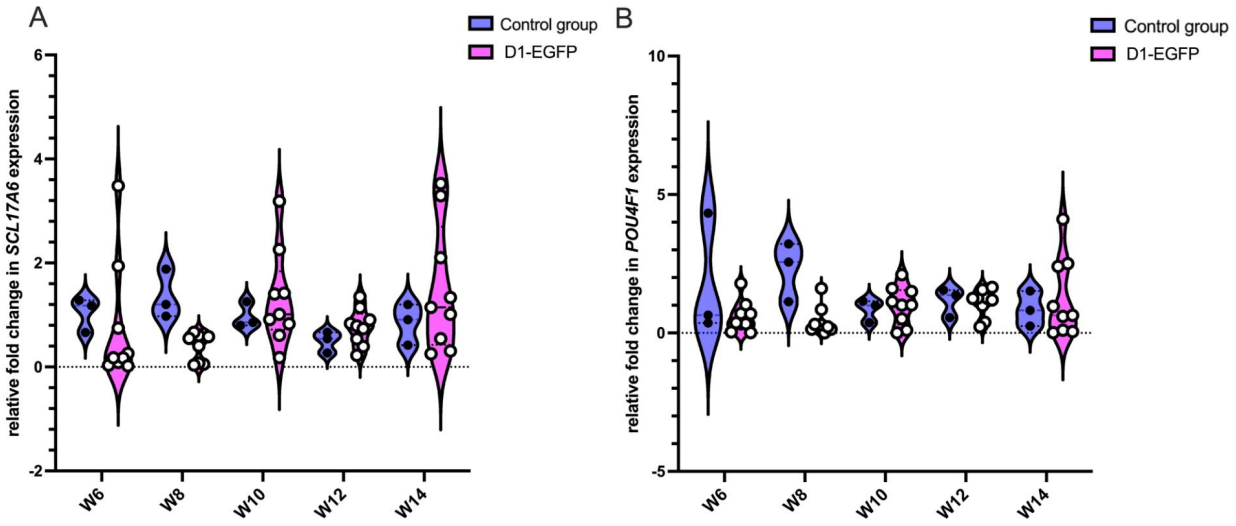

Fig. 16: The relative fold change in *SCL17A6* gene (A) and *POU4F1* gene (B) expression in ROs at different time points. All data were normalized to the control group at W6. N=3, n=3 for control group; N=9, n=3 for D1-EGFP group, 2-way ANOVA test was performed, p value is not significant. Image was generated using Graphpad Prism 9.

4. Discussion

In this study, we used synthetic promoters A1 and D1 to specifically target cones and RGCs within 3D stem cell-derived ROs to allow live cell imaging of their development, which has not been fully explored in ROs. Our primary goal was to observe the emergence of cones and RGCs within ROs and to validate these observations by IHC.

Additionally, given the tendency of RGCs in ROs to undergo early necrosis and the lack of documented birth timelines for RGCs within living ROs, we integrated qRT-PCR and FC for further validation. Because the efficacy of synthetic promoters for targeting retinal cells in ROs derived from the B7 cell line has not been thoroughly evaluated, we also tested their applications in ROs.

4.1 Live-cell imaging for retinal cells

The developmental stages of RGCs and cones, individually derived from D1-EGFP ROs and A1-tdTomato ROs, were periodically imaged and stained over time using live-cell fluorescence microscopy and IHC. Under live-cell imaging, the emergence of RGCs at W7, the peak of RGCs at W12, and the decline of RGCs after W12 aligned with previous study by Wahle et al. (2023). Also, the observation in FC analysis also showed a similar trend (Fig. 14). As independent entities, the ROs do not possess any other projections to the outer world and are not vascularized. Thus, the reduction in RGC numbers due to RGC core necrosis reported by previous studies can be further confirmed in this study (Aparicio et al., 2017; Capowski et al., 2019; Lancaster et al., 2013; Wahlin et al., 2017; Zhong et al., 2014). Additionally, the multiple forms of RGCs observed in ROs might indicate different subtypes of RGCs (Fig. 3a and Fig. 11b). The categorization of RGC subtype was traditionally achieved by distinguishing their dendritic morphology with their arborization in IPL and soma size (Dhande et al., 2015; Sanes and Masland, 2015). Nevertheless, the IPL is not yet fully developed at early stages like in this study, thus, the arborization in IPL cannot be identified. It has been previously shown that

the synthetic promoter D1 is specific in targeting a cluster of bistratified RGCs in mice interacting with ACs in the IPL (Jüttner et al., 2019). In this study, the feasibility of synthetic promoter D1 in the human B7 cell line to target RGCs was demonstrated through identifying their position in the GCL and expression of EGFP signal. However, whether the synthetic promoter D1 also labels the bistratified RGCs or other subtypes of RGCs remained unverifiable via live cell imaging alone. The resolution of the fluorescence microscope used in this experiment is lower than that of light-sheet fluorescence microscopy, that enables further detail for large samples and observations of three-dimensional for the long-term examination, as said by Stelzer et al.(2021).

The synthetic promoter A1 was proven to be specific for cones in mice (Jüttner et al., 2019). In this study, the cones were identified by the fluorescent signal and position in the ONL, which confirmed the feasibility of promoter A1 in human B7 cell lines. The appearance of cones at W14 is also consistent with earlier study (Fig. 3c). As mentioned earlier, the B7 cell lines after nucleofection were selected through the antibiotic resistence. Theoretically, the ROs contain successfully transfected stem cells, and as the RGCs within ROs developed over time, the red signal for cones would be detecTab. throughout the ONL, while the green signal for RGCs should be present throughout the GCL. However, not all ROs were observed expressing fluorescent signals. Additionally, discontinuous expression of tdTomato signal in cones within the ONL, as well as the EGFP signal in RGCs within the GCL was also observed. A highly plausibel reason for this observation could be the epigenetic silencing of the transgene (Bintu et al., 2016; Hathaway et al., 2012; Vaissière et al., 2008). If the transgenes were integrated into a CpG-rich genomic region, they might be more susceptible to DNA-methylation and histone deacetylation that lead to the eventual loss of expression of the genes of interest (Reina and Cavalieri, 2020; Smith and Shilatifard, 2010; Uruci et al., 2021). A low dose of demethylation treatment with 5-Aza-2'-deoxycytidine can be useful for reducing DNA methylation level (Christman,

2002; Daskalakis et al., 2002). Moreover, integrations into heterochrimatic, repressive genomic loci can also lead to transgene silencing (Lensch et al., 2021).

4.2 Visualization of retinal cells using Immunohistochemistry

The IHC labeled RGCs with anti-POU4F1 antibody and cones with the anti-Recoverin antibody. Coupling the fluorescent label with the retinal cell specific marker confirms the presence of the desired retinal cell type.

The fact that there were few coincident POU4F1+/GFP+ RGCs and many GFP+ RGCs without POU4F1 expression suggests that the synthetic promoter D1 might label only a subset of the RGCs. This conclusion also explains the observations from live-cell imaging that the GFP+ RGCs were not uniformly distributed in the GCL. According to previous studies, RGCs represent a heterogeneous population that consists of over 30 subtypes. Most RGC pan markers are expressed across several subtypes, with none displaying predominance over the others (Dhande et al., 2015; Langer et al., 2018; Rheaume et al., 2018; Sanes and Masland, 2015). Furthermore, it was reported by Nadal-Nicolas et al. (2009) that POU4F1 is expressed in 92.2 % of the RGCs in rat retinas, while the most ipRGCs and RGCs projecting ipsilaterally do not express POU4F1 (Nadal-Nicolas et al. 2012). Therefore, the tendency of expressing less or no POU4F1 is likely due to the selectivity of the synthetic promoter D1. The POU4F+ / GFP+ RGCs in IHC displayed a clear morphology with axons extending, which also corresponded to the observation from live cell imaging, further confirming the successful expression driven by the D1 promoter. This experiment can be further improved by testing other RGC-specific markers, which may identify other subtypes of RGCs driven by promoter D1. For example, subtypes not recognized by POU4F1 may be identified by RBPMS as it has been suggested to label nearly the whole RGC population (Meng et al., 2024; Rodriguez et al., 2014). However, compared to other markers, the RBPMS is less frequently expressed during the early developmental stages, and thus, this might underestimate the RGC population at such stages like in this study (Langer et al., 2018). Although the current research cannot

precisely categorize each subtype, it has been reported that the intermediate subgroups might be classified using specific markers such as Runx1, Fst, and Zic (Rheaume et al., 2018). A more exact classification of RGCs subtypes derived from synthetic promoter D1 can be analyzed using single-cell sequencing as the study of RGCs subtype allows uncovering specific signaling way (Langer et al., 2018).

It is already known that the cones appear earlier than the rods (Lu et al., 2020; Wahle et al., 2023) (Fig. 1.3 c). The recoverin+/ tdTomato+ cells could be thereby identified as cones in the IHC at W13. Additionally, the recoverin staining of cones, mainly located in OS, also aligned with a previous finding (Zang and Neuhauss, 2018). Another potential staining method for cones could involve using the Arrestin 3, which is a specific marker for cones (Krupnick and Benovic,1998; Jüttner et al., 2019). The Arrestin 3 would be useful for distinguishing cones from rods in IHC at later developmental stages.

4.3 Detecting fluorescent marker of RGC and assessing transcriptional level of RGC during *in vitro* retinogenesis

In the FC analysis, the increase from W6 to W10 and then the abrupt decrease in GFP+ cells from W12 to W14 were aligned with the observation in live-cell imaging indicating RGC loss at a later stage. Apart from the previously mentioned epigenetic silencing, the variation of the percentage of GFP+ cells among samples in the experimental group can be attributed to a phenomenon known as batch effects, which arise from differences in experimental batches, including laboratory conditions, different reagent batches, and personnel variations in handling techniques (Leek et al., 2010). While statistical methods exist to normalize data in experiments with large sample sizes, there is no suiTab. method for small sample sizes, and batch effects are ineviTab.. Moreover, the control group without fluorescent reporter gene should not exhibit any fluorescent signals throughout the entire period. However, it showed a positive GFP signal in one sample of the control group in FC at W14. This can be explained as an autofluorescent background signal resulting from cell death. The metabolic processes that are characteristic of living cells are disrupted when cells die, which results in the accumulation of specific metabolic products,

including nicotinamide adenine dinucleotide phosphate (NADP) and lipofuscin (Bartolomé and Abramov, 2015). The aforementioned molecules are capable of emitting fluorescence when stimulated by specific light wavelengths employed in FC (Monici ,2005). In the analysis of FC data, the identification of cell debris is commonly based on light scattering properties. It has been shown that a low forward scatter (FSC) indicates a smaller cell volume, while a high side scatter (SSC) reflects increased cell granularity in FC, which indicates cell death (Koopman et al., 1994; Reardon et al., 2014). Therefore, the FSC and SSC magnitude for our data can be adjusted to exclude the autofluorescent cell debris, providing a more reliable result. Similar gating strategies have been reported by Mancuso et al. (2014), where negative gating using FSC versus SSC was employed to exclude cell debris and dead cells.

When compared to FC, there was an inconsistency in the corresponding qRT-PCR analysis, as GFP expression was significantly increased and was observed to be at its highest overall expression level at W14. This discrepancy can be attributed to the fact that FC detects at the translational level, whereas qRT-PCR measures at the transcriptional level. In eukaryotes, transcribed mRNA is not translated into protein until it reaches the cytoplasm, where it undergoes complex modifications (Clancy and Brown, 2008). Therefore, the transcriptional level is not directly correlated to the translation level.

In addition to the GFP primer mentioned above, two other primers were used in the RT-qPCR, each targeting *POU4F1* and *SCL17A6*. No significant differences in *POU4F1* and *SCL17A6* expression were observed between the experimental group and the wild type, consistent with the expectation that there should be no difference in retinal cell development between the control groups and experimental groups under the same condition. It was also observed that there was a generally low fold change in all three gene expressions. This may be due to the dilution of RGC mRNA concentration during development as other retinal cell types begin to appear, reducing the proportion of RGCs as the amount of RGCs remains sTab. while more other cell types continue to appear. It can be seen that some samples in both groups have higher expression levels of *POU4F1* and *SCL17A6* at W6 and W8 compared to later weeks. In general, the

expression levels of GFP, *POU4F1* and *SCL17A6* showed an overall increasing expression level over time, in line with RGC development, indicating a successful introduction of the synthetic promoter D1.

4.4 Outlook for future use of the generated cell lines synthetic promoters

As previously stated, the feasibility of utilizing the D1-EGFP and A1-tdTomato cell lines has been demonstrated. It offers a number of potential avenues for furthering our research on retinal cells. The time line of RGC development has been tested with this approach and can now be used as baseline for other protocols that provide accelerated growth, maturation or vascularization (please add papers where they show similar). Another approach could be that the specific fluorescent signal of the targeted cells can be used to precisely sort the required cells using fluorescence-activated cell sorting (FACS), which offers an opportunity for cell replacement therapy. Studies by Lamba et al. (2010) and Sluch et al. (2015) have demonstrated the potential of utilizing purified PRs and RGCs through the FACS technique for cell replacement therapy. Overall, the reporter cell lines have been validated in my thesis and they will be used for further RO research in the Busskamp laboratory.

5. Summery

In this study, I successfully tracked and confirmed the emergence of cones at week 13 using live cell imaging and immunohistochemistry. The successful real-time tracking of retinal cells in retinal organoids using fluorescent labels is confirmed to be a convenient way to quickly check the developmental status of cells of interest. The emergence of retinal ganglion cells at wee 7, their peak abundance at week12, and their subsequent decline from week 14 were also documented in the same manner and further validated by Real-Time Quantitative Reverse Transcription polymerase chain reaction and flow cytometry. Furthermore, the feasibility of the two synthetic promoters A1 and D1 in the human B7 cell line is confirmed by the successful targeting of retinal cells.

A baseline growth curve of retinal ganglion cells was established for retinal ganglion cells in B7 stem cell-derived retinal organoids. The trend obtained serves as a short parameter for further experiments and can be used as a negative control to evaluate the survival of retinal ganglion cells under different conditions in retinal organoids, such as the vascularization of retinal organoids. In addition, D1-promoter-driven retinal ganglion cells are likely to represent specific subtypes that do not express the retinal ganglion cell marker Pit-Oct-Unc class 4 homeobox. This limits their generalization to all retinal ganglion cell populations.

In addition, four constructs, each labeled with a different reporter gene, were generated using alternative synthetic promoters targeting other retinal cell types. After nucleofection and selection, the constructs were cryopreserved for future analysis in the Busskamp.

6. List of figures

7. List of tables

8. References

Achberger K, Probst C, Haderspeck J, Bolz S, Rogal J, Chuchuy J, et al. Merging organoid and organ-on-a-chip technology to generate complex multi-layer tissue models in a human retina-on-a-chip platform. *Elife.* 2019;8:e46188.

Aparicio JG, Hopp H, Choi A, Mandayam Comar J, Liao VC, Harutyunyan N, Lee TC. 2017. Temporal expression of CD184(CXCR4) and CD171(L1CAM) identifies distinct early developmental stages of human retinal ganglion cells in embryonic stem cell derived retina. Exp Eye Res 154:177–189.

Badea TC, Nathans J. Quantitative analysis of neuronal morphologies in the mouse retina visualized by using a genetically directed reporter. *J Comp Neurol.* 2004 Dec 20;480(4):331-51. doi: 10.1002/cne.20304. PMID: 15558785.

Baden T, Berens P, Franke K, Román Rosón M, Bethge M, Euler T. The functional diversity of retinal ganglion cells in the mouse. *Nature.* 2016 Jan 21;529(7586):345-50. doi: 10.1038/nature16468. PMID: 26735013; PMCID: PMC4724341.

Bae JA, Mu S, Kim JS, Turner NL, Tartavull I, Kemnitz N, Jordan CS, Norton AD, Silversmith WM, Prentki R, Sorek M, David C, Jones DL, Bland D, Sterling ALR, Park J, Briggman KL, Seung HS; Eyewirers. Digital museum of retinal ganglion cells with dense anatomy and physiology. *Cell.* 2018 May 17;173(5):1293-1306.e19. doi: 10.1016/j.cell.2018.04.040. PMID: 29775596; PMCID: PMC6556895.

BarnsTab. CJ, Dräger UC Thy-1 antigen: a ganglion cell-specific marker in rodent retina. *Neuroscience.* 1984 Apr;11(4):847-55. doi: 10.1016/0306-4522(84)90195-7. PMID: 6146113.

Bartolomé F, Abramov AY. Measurement of mitochondrial NADH and FAD autofluorescencefluorescence in live cells. Methods Mol Biol. 2015; 1264:263-70. doi: 10.1007/978-1-4939-2257-4_23. PMID: 25631020.

Bintu L, Yong J, Antebi YE, McCue K, Kazuki Y, Uno N, Oshimura M, Elowitz MB. Dynamics of epigenetic regulation at the single-cell level. Science. 2016 Feb 12;351(6274):720-4. doi: 10.1126/science. aab2956. PMID: 26912859; PMCID: PMC5108652.

Bowmaker JK, Hunt DM Evolution of vertebrate visual pigments. *Curr Biol.*

Cui, Q., Ren, C., Sollars, P. J., Pickard, G. E., & So, K. F. (2015). The injury resistant ability of melanopsin-expressing intrinsically photosensitive retinal ganglion cells. *Neuroscience*, *284*, 845-853.

Dacey DM, Peterson BB, Robinson FR, Gamlin PD.Fireworks in the primate retina: in vitro photodynamics reveals diverse LGN-projecting ganglion cell types. *Neuron.* 2003;37(1):15-27.

Daskalakis M, Tudung T. Nguyen, Carvell Nguyen, Per Guldberg, Gabriele Köhler, Pierre Wijermans, Peter A. Jones, Michael Lübbert; Demethylation of a hypermethylated P15/INK4B gene in patients with myelodysplastic syndrome by 5-Aza-2′-deoxycytidine (decitabine) treatment. *Blood* 2002; 100 (8): 2957–2964.

Dhande OS, Huberman AD. Retinal ganglion cell maps in the brain: implications forvisual processing. *Curr Opin Neurobiol.* 2014;24:133–142. doi: 10.1016/j.conb.2013.08.006.

Dhande OS, Stafford BK, Lim JA, Huberman AD. Contributions of Retinal Ganglion Cells to Subcortical Visual Processing and Behaviors. Annu Rev Vis Sci. 2015 Nov 24;1:291- 328. doi: 10.1146/annurev-vision-082114-035502. PMID: 28532372.

DiStefano, T.; Chen, H.Y.; Panebianco, C.; Kaya, K.D.; Brooks, M.J.; Gieser, L.; Morgan, N.Y.; Pohida, T.; Swaroop, A. Accelerated and Improved Differentiation of Retinal Organoids from Pluripotent Stem Cells in Rotating-Wall Vessel Bioreactors. *Stem Cell Rep.* **2018**, *10*, 300–313.

Eiraku M, Takata N, Ishibashi H, Kawada M, Sakakura E, Okuda S, Sekiguchi K, Adachi T, Sasai Y. Self-organizing optic-cup morphogenesis in three-dimensional culture. Nature.
2011 Apr 7;472(7341):51-6. doi: 10.1038/nature09941. PMID: 21475194.

Eiraku M, **Sasai Y.** 2011. Mouse embryonic stem cell culture for generation of three-dimensional retinal and cortical tissues. Nat Protoc 7:69–79.

Esrefoglu M. Role of stem cells in repair of liver injury: experimental and clinical benefit of transferred stem cells on liver failure. World J Gastroenterol. 2013 Oct 28;19(40):6757- 73. doi: 10.3748/wjg.v19.i40.6757. PMID: 24187451; PMCID: PMC3812475.

Euler, T., Haverkamp, S., Schubert, T. *et al.* Retinal bipolar cells: elementary building blocks of vision. *Nat Rev Neurosci* **15**, 507–519 (2014).

Evans MJ, **Kaufman MH**. Establishment in culture of pluripotential cells from mouse embryos. Nature. 1981 Jul 9;292(5819):154-6. doi: 10.1038/292154a0. PMID: 7242681.

Fradot M, Busskamp V, Forster V, Cronin T, Léveillard T, Bennett J, Sahel JA, Roska B, Picaud S. Gene therapy in ophthalmology: validation on cultured retinal cells and explants from postmortem human eyes. Hum Gene Ther. 2011 May;22(5):587-93. doi: 10.1089/hum.2010.157. Epub 2011 Feb 26. PMID: 21142470.

Gao L, Chen X, Zeng Y, Li Q, Zou T, et al. Intermittent high oxygen influences the formation of neural retinal tissue from human embryonic stem cells. Sci Rep. 2016;6:29944. doi: 10.1038/srep29944.

Gasparini, S.J.; Llonch, S.; Borsch, O.; Ader, M. Transplantation of Photoreceptors into the Degenerative Retina: Current State and Future Perspectives. *Prog. Retin. Eye Res.* 2019, *69*, 1–37.

Gollisch T, Meister M. Eye smarter than scientists believed: neural computations in circuits of the retina. *Neuron.* 2010 Jan 28;65(2):150-64. doi: 10.1016/j.neuron.2009.12.009. PMID: 20152123; PMCID: PMC3717333

Hallam, D.; Hilgen, G.; Dorgau, B.; Zhu, L.; Yu, M.; Bojic, S.; Hewitt, P.; Schmitt, M.; Uteng, M.; Kustermann, S.; et al. Human-Induced Pluripotent Stem Cells Generate Light Responsive Retinal Organoids with Variable and Nutrient-Dependent Efficiency. *Stem Cells* **2018**, *36*, 1535–1551.

Hamel C. Retinitis pigmentosa. Orphanet J Rare Dis. 2006;1:40. doi: 10.1186/1750-1172- 1-40.

Hathaway NA, Bell O, Hodges C, Miller EL, Neel DS, Crabtree GR. Dynamics and memory of heterochromatin in living cells. Cell. 2012 Jun 22;149(7):1447-60. doi: 10.1016/j.cell.2012.03.052. Epub 2012 Jun 14. PMID: 22704655; PMCID: PMC3422694.

Hirami Y, Osakada F, Takahashi K, Okita K, Yamanaka S, Ikeda H, Yoshimura N, Takahashi M. Generation of retinal cells from mouse and human induced pluripotent stem cells. Neurosci Lett. 2009 Jul 24;458(3):126-31. doi: 10.1016/j.neulet.2009.04.035. Epub 2009 Apr 18. PMID: 19379795.

Huch M, Dorrell C, Boj SF, van Es JH, Li VS, van de Wetering M, Sato T, Hamer K, Sasaki N, Finegold MJ, Haft A, Vries RG, Grompe M, Clevers H. In vitro expansion of single Lgr5+ liver stem cells induced by Wnt-driven regeneration. Nature. 2013 Feb 14;494(7436):247- 50. doi: 10.1038/nature11826. Epub 2013 Jan 27. PMID: 23354049; PMCID: PMC3634804.

Hunt, N.C.; Hallam, D.; Karimi, A.; Mellough, C.B.; Chen, J.; Steel, D.H.W.; Lako, M. 3D Culture of Human Pluripotent Stem Cells in RGD-Alginate Hydrogel Improves Retinal Tissue Development. *Acta Biomater.* **2017**, *49*, 329–343.

Ito, S.; Onishi, A.; Takahashi, M. Chemically-Induced Photoreceptor Degeneration and Protection in Mouse IPSC-Derived Three-Dimensional Retinal Organoids. *Stem Cell Res.* **2017**, *24*, 94–101.

Jüttner J, Szabo A, Gross-Scherf B, Morikawa RK, Rompani SB, Hantz P, Szikra T, Esposti F, Cowan CS, Bharioke A, Patino-Alvarez CP, Keles Ö, Kusnyerik A, Azoulay T, Hartl D, Krebs AR, Schübeler D, Hajdu RI, Lukats A, Nemeth J, Nagy ZZ, Wu KC, Wu RH, Xiang L, Fang XL, Jin ZB, Goldblum D, Hasler PW, Scholl HPN, Krol J, Roska B. Targeting neuronal and glial cell types with synthetic promoter AAVs in mice, non-human primates and humans. Nat Neurosci. 2019 Aug;22(8):1345-1356. doi: 10.1038/s41593-019-0431- 2. Epub 2019 Jul 8. PMID: 31285614.

Kawamura S. Rhodopsin phosphorylation as a mechanism of cyclic GMP phosphodiesterase regulation by S-modulin. *Nature.* 1993 Apr 29;362(6423):855–857. doi: 10.1038/362855a0.

Keltner JL, Roth AM, Chang RS. Photoreceptor degeneration. Possible autoimmune disorder. *Arch Ophthalmol.* 1983 Apr;101(4):564–569. doi: 10.1001/archopht.1983.01040010564006.

Khan, M.; Arno, G.; Fakin, A.; Parfitt, D.A.; Dhooge, P.P.A.; Albert, S.; Bax, N.M.; Duijkers, L.; Niblock, M.; Hau, K.L.; et al. Detailed Phenotyping and Therapeutic Strategies for Intronic ABCA4 Variants in Stargardt Disease. *Mol. Ther. Nucleic Acids* **2020**, *21*, 412–427

Kim U S, Mahroo OA, Mollon JD, Yu-Wai-Man P. Retinal Ganglion Cells—Diversity of Cell Types and Clinical Relevance. *Front Neurol*. 2021;12:661938. doi: 10.3389/fneur.2021.661938.

Koopman G, Reutelingsperger CP, Kuijten GA, Keehnen RM, Pals ST, van Oers MH. Annexin V for flow cytometric detection of phosphatidylserine expression on B cells undergoing apoptosis. Blood. 1994 Sep 1;84(5):1415-20. PMID: 8068938.

Krohne, T.U.; Westenskow, P.D.; Kurihara, T.; Friedlander, D.F.; Lehmann, M.; Dorsey, A.L.; Li, W.; Zhu, S.; Schultz, A.; Wang, J.; et al. Generation of Retinal Pigment Epithelial Cells from Small Molecules and OCT4 Reprogrammed Human Induced Pluripotent Stem Cells. *Stem Cells Transl. Med.* **2012**, *1*, 96–109.

Krupnick JG, Benovic JL. The role of receptor kinases and arrestins in G protein-coupled receptor regulation. Annu Rev Pharmacol Toxicol. 1998;38:289-319. doi: 10.1146/annurev.pharmtox.38.1.289. PMID: 9597157.

Kuffler SW. Discharge patterns and functional organization of mammalian retina. *J Neurophysiol.* 1953;16:37–68. doi: 10.1152/jn.1953.16.1.37.

Lamba DA, Karl MO, Ware CB, Reh TA. Efficient generation of retinal progenitor cells from human embryonic stem cells. Proc Natl Acad Sci U SA. 2006 Aug 22;103(34):12769-74. doi: 10.1073/pnas.0601990103. Epub 2006 Aug 14. PMID: 16908856; PMCID: PMC1568922.

Lamba DA, McUsic A, Hirata RK, Wang PR, Russell D, Reh TA. Generation, purification and transplantation of photoreceptors derived from human induced pluripotent stem cells. PLoS One. 2010 Jan 20;5(1): e8763. doi: 10.1371/journal.pone.0008763. PMID: 20098701; PMCID: PMC2808350.

Lancaster MA, Renner M, Martin CA, Wenzel D, Bicknell LS, Hurles ME, Homfray T, Penninger JM, Jackson AP, Knoblich JA. Cerebral organoids model human brain development and microcephaly. Nature. 2013 Sep 19;501(7467):373-9. doi: 10.1038/nature12517. Epub 2013 Aug 28. PMID: 23995685; PMCID: PMC3817409.

Langer KB, Ohlemacher SK, Phillips MJ, Fligor CM, Jiang P, Gamm DM, Meyer JS. Retinal Ganglion Cell Diversity and Subtype Specification from Human Pluripotent Stem Cells. Stem Cell Reports. 2018 Apr

10;10(4):1282-1293. doi: 10.1016/j.stemcr.2018.02.010. Epub 2018 Mar 22. PMID: 29576537; PMCID: PMC5998302.

Leek, J., Scharpf, R., Bravo, H. *et al.* Tackling the widespread and critical impact of batch effects in high-throughput data. *Nat Rev Genet* **11**, 733–739 (2010).

Lensch S, Herschl MH, Ludwig CH, Sinha J, Hinks MM, Mukund A, Fujimori T, and Bintu L (2021). Dynamic spreading of chromatin-mediated gene silencing and reactivation between neighboring genes in single cells. bioRxiv, 2021.11.04.467237. 10.1101/2021.11.04.467237.

Li JQ, Welchowski T, Schmid M, Mauschitz MM, Holz FG, Finger RP. Prevalence and incidence of age-related macular degeneration in Europe: a systematic review and meta-analysis. Br J Ophthalmol. 2020 Aug;104(8):1077-1084. doi: 10.1136/bjophthalmol-2019-314422. PMID: 31712255

Meng M, Chaqour B, O'Neill N, Dine K, Sarabu N, Ying GS, Shindler KS, Ross AG. Comparison of Brn3a and RBPMS Labeling to Assess Retinal Ganglion Cell Loss During Aging and in a Model of Optic Neuropathy. Invest Ophthalmol Vis Sci. 2024 Apr 1;65(4):19. doi: 10.1167/iovs.65.4.19. PMID: 38587440; PMCID: PMC11005068.

Meyer JS, Shearer RL, Capowski EE, Wright LS, Wallace KA, McMillan EL, Zhang SC, Gamm DM. 2009. Modeling early retinal development with human embryonic and induced pluripotent stem cells. Proc Natl Acad Sci U S A 106:16698–16703.

Monici M. Cell and tissue autofluorescencefluorescence research and diagnostic applications. Biotechnol Annu Rev. 2005; 11:227-56. doi: 10.1016/S1387-2656(05)11007-2. PMID: 16216779.

Mustafi D, Engel AH, Palczewski K. Structure of cone photoreceptors. *Prog Retin Eye Res.* 2009 Jul;28(4):289-302. doi: 10.1016/j.preteyeres.2009.05.003. PMID: 19501669; PMCID: PMC2740621.

Muzumdar MD, Tasic B, Miyamichi K, Li L, Luo L. A global double-fluorescent Fluorescent Cre reporter mouse. Genesis. 2007 Sep;45(9):593-605. doi: 10.1002/dvg.20335. PMID: 17868096.

Nadal-Nicolas FM, Jimenez-Lopez M, Salinas-Navarro M, Sobrado-Calvo P, Alburquerque-Bejar JJ, Vidal-Sanz M, Agudo-Barriuso M. Whole number, distribution and co-expression of brn3 transcription factors in retinal ganglion cells of adult albino and pigmented rats. Plos One. 2012;7:e49830. doi: 10.1371/journal.pone.0049830.

Nadal-Nicolas FM, Jimenez-Lopez M, Sobrado-Calvo P, Nieto-Lopez L, Canovas- Martinez I, Salinas-Navarro M, Vidal-Sanz M, Agudo M. Brn3a as a Marker of Retinal Ganglion Cells: Qualitative and Quantitative Time Course Studies in Naive and Optic Nerve-Injured Retinas. Investigative Ophthalmology & Visual Science. 2009;50:3860– 3868. doi: 10.1167/iovs.08-3267.

Nakano T, Ando S, Takata N, Kawada M, Muguruma K, Sekiguchi K, Saito K, Yonemura S, Eiraku M, Sasai Y. 2012. Self-formation of optic cups and storable stratified neural retina from human ESCs. Cell Stem Cell 10:771–785.

Nakatsuji, N., Nakajima, F. & Tokunaga, K. HLA-haplotype banking and iPS cells. *Nat Biotechnol* **26**, 739–740 (2008).

O'Hara-Wright M, Gonzalez-Cordero A. Retinal organoids: a window into human retinal development. Development. 2020 Dec 24;147(24): dev189746. doi: 10.1242/dev.189746. PMID: 33361444; PMCID: PMC7774906.

Okabe M, Ikawa M, Kominami K, Nakanishi T, Nishimune Y. 'Green mice' as a source of ubiquitous green cells. FEBS Lett. 1997 May 5;407(3):313-9. doi: 10.1016/s0014- 5793(97)00313-x. PMID: 9175875.

Osakada F, Jin ZB, Hirami Y, Ikeda H, Danjyo T, Watanabe K, Sasai Y, Takahashi M. In vitro differentiation of retinal cells from human pluripotent stem cells by small-molecule induction. J Cell Sci. 2009 Sep 1;122(Pt 17):3169-79. doi: 10.1242/jcs.050393. Epub 2009 Aug 11. PMID: 19671662.

Oswald J, Kegeles E, Minelli T, Volchkov P, Baranov P. Transplantation of miPSC/mESC- derived retinal ganglion cells into healthy and glaucomatous retinas. Mol Ther Methods Clin Dev. 2021 Mar 10;21:180-198. doi: 10.1016/j.omtm.2021.03.004. PMID: 33816648; PMCID: PMC7994731.

Ovando-Roche, P.; West, E.L.; Branch, M.J.; Sampson, R.D.; Fernando, M.; Munro, P.; Georgiadis, A.; Rizzi, M.; Kloc, M.; Naeem, A.; et al. Use of Bioreactors for Culturing Human Retinal Organoids Improves Photoreceptor Yields. *Stem Cell Res. Ther.* **2018**, *9*, 156.

Pearson AA. The development of the eyelids. Part I. External features. *J Anat.* 1980 Jan;130(Pt 1):33-42. PMID: 7364662; PMCID: PMC1233106.

Peng YR, Shekhar K, Yan W, Herrmann D, Sappington A, Bryman GS, van Zyl T, Do MTH, Regev A, Sanes JR. Molecular classification and comparative taxonomics of foveal and peripheral cells in primate retina. *Cell.* 2019 Feb 21;176(5):1222-1237.e22. doi: 10.1016/j.cell.2019.01.004. PMID: 30712875; PMCID: PMC6424338.

Pera M.F., Susan Cooper, Judith Mills, Jennifer M. Parrington, Isolation and characterization of a multipotent clone of human embryonal carcinoma cells, Differentiation, Volume 42, Issue 1,1989, Pages 10-23, ISSN 0301-4681.

Rapaport DH, Wong LL, Wood ED, Yasumura D, LaVail MM. Timing and topography of cell genesis in the rat retina. J Comp Neurol. 2004 Jun 21;474(2):304-24. doi: 10.1002/cne.20134. PMID: 15164429.

Reardon AJF, Elliott JAW, McGann LE. Fluorescence as an alternative to light-scatter gating strategies to identify frozen–thawed cells with flow cytometry. Cryobiology 2014;69:91–99

Reichenbach A, Bringmann A. New functions of Müller cells. Glia. 2013 May;61(5):651- 78. doi: 10.1002/glia.22477. Epub 2013 Feb 26. PMID: 23440929.

Reina C, and **Cavalieri V** (2020). Epigenetic Modulation of Chromatin States and Gene Expression by G-Quadruplex Structures. Int. J. Mol. Sci. 21. 10.3390/ijms21114172.

Rheaume, B.A., Jereen, A., Bolisetty, M. *et al.* Single cell transcriptome profiling of retinal ganglion cells identifies cellular subtypes. *Nat Commun* **9**, 2759 (2018).

Rodriguez AR, de Sevilla Müller LP, Brecha NC. The RNA binding protein RBPMS is a selective marker of ganglion cells in the mammalian retina. J Comp Neurol. 2014 Apr 15;522(6):1411-43. doi: 10.1002/cne.23521. PMID: 24318667; PMCID: PMC3959221.

Roorda A, Metha AB, Lennie P, Williams DR. Packing arrangement of the three cone classes in primate retina. *Vision Res.* 2001;41:1291–1306. doi: 10.1016/s0042- 6989(01)00043-8.

Sanes JR, Masland RH. The types of retinal ganglion cells: current status and implications for neuronal classification. Annu Rev Neurosci. 2015 Jul 8; 38:221-46. doi: 10.1146/annurev-neuro-071714-034120. Epub 2015 Apr 9. PMID: 25897874.

Schorpp M, Jäger R, Schellander K, Schenkel J, Wagner EF, Weiher H, Angel P. The human ubiquitin C promoter directs high ubiquitous expression of transgenes in mice.

Nucleic Acids Res. 1996 May 1;24(9):1787-8. doi: 10.1093/nar/24.9.1787. PMID: 8650001; PMCID: PMC145851.

Sharma, T.P.; Wiley, L.A.; Whitmore, S.S.; Anfinson, K.R.; Cranston, C.M.; Oppedal, D.J.; Daggett, H.T.; Mullins, R.F.; Tucker, B.A.; Stone, E.M. Patient-Specific Induced Pluripotent Stem Cells to Evaluate the Pathophysiology of TRNT1-Associated Retinitis Pigmentosa. *Stem Cell Res.* **2017**, *21*, 58–70.

Shelley EJ, Madigan MC, Natoli R, Penfold PL, Provis JM. Cone degeneration in aging and age-related macular degeneration. *Arch Ophthalmol.* 2009;127:483–492. doi: 10.1001/archophthalmol.2008.622.

Shimada, H.; Lu, Q.; Insinna-Kettenhofen, C.; Nagashima, K.; English, M.A.; Semler, E.M.; Mahgerefteh, J.; Cideciyan, A.V.; Li, T.; Brooks, B.P.; et al. In Vitro Modeling Using Ciliopathy-Patient-Derived Cells Reveals Distinct Cilia Dysfunctions Caused by CEP290 Mutations. *Cell Rep.* **2017**, *20*, 384–396.

Shimomura O, Johnson FH, Saiga Y. Extraction, purification and properties of aequorin, a bioluminescent protein from the luminous hydromedusan, Aequorea. J Cell Comp Physiol. 1962 Jun; 59:223-39. doi: 10.1002/jcp.1030590302. PMID: 13911999.

Singh RK, Mallela RK, Cornuet PK, Reifler AN, Chervenak AP, West MD, Wong KY, Nasonkin IO. Characterization of three-dimensional retinal tissue derived from human embryonic stem cells in adherent monolayer cultures. Stem Cells Dev. 2015;24:2778-2795. doi: 10.1089/scd.2015.0144.

Sluch VM, Davis CH, Ranganathan V, Kerr JM, Krick K, Martin R, Berlinicke CA, Marsh-Armstrong N, Diamond JS, Mao HQ, Zack DJ. 2015. Differentiation of human ESCs to retinal ganglion cells using a CRISPR engineered reporter cell line. Sci Rep 5:16595.

Smith E, and **Shilatifard** A (2010). The chromatin signaling pathway: diverse mechanisms of recruitment of histone-modifying enzymes and varied biological outcomes. Mol. Cell 40, 689–701.

Sridhar A, Hoshino A, Finkbeiner CR, Chitsazan A, Dai L, Haugan AK, Eschenbacher KM, Jackson DL, Trapnell C, Bermingham-McDonogh O, et al. Single-cell transcriptomic comparison of human fetal retina, hPSC-derived retinal organoids, and long-term retinal cultures. *Cell Rep.* 2020;30:1644. doi: 10.1016/j.celrep.2020.01.007.

Stelzer, E.H.K., Strobl, F., Chang, BJ. *et al.* Light sheet fluorescencefluorescence microscopy. *Nat Rev Methods Primers* **1**, 73 (2021).

Strauss O. The retinal pigment epithelium in visual function. Physiol Rev. 2005 Jul;85(3):845-81. doi: 10.1152/physrev.00021.2004. PMID: 15987797.

Sugihara, H., Toda, S., Miyabara, S., Fujiyama, C., & Yonemitsu, N. (1993). Reconstruction of alveolus-like structure from alveolar type II epithelial cells in three- dimensional collagen gel matrix culture. *The American journal of pathology*, *142*(3), 783

Surridge AK, Osorio D, Mundy NI. Evolution and selection of trichromatic vision in primates. *Trends Ecol Evol.* 2003;18(4):198-205. doi: 10.1016/s0169-5347(03)00012-0.

Szatko KP, Korympidou MM, Ran Y, et al. Neural circuits in the mouse retina support color vision in the upper visual field. *Nat Commun.* 2020;11:3481. doi: 10.1038/s41467-020-17306-0.

Takahashi K, Tanabe K, Ohnuki M, Narita M, Ichisaka T, Tomoda K, Yamanaka S. Induction of pluripotent stem cells from adult human fibroblasts by defined factors. Cell. 2007 Nov 30;131(5):861-72. doi: 10.1016/j.cell.2007.11.019. PMID: 18035408.

Takahashi K, Yamanaka S. Induction of pluripotent stem cells from mouse embryonic and adult fibroblast cultures by defined factors. Cell. 2006 Aug 25;126(4):663-76. doi: 10.1016/j.cell.2006.07.024. Epub 2006 Aug 10. PMID: 16904174.

Tran NM, Shekhar K, Whitney IE, Jacobi A, Benhar I, Hong G, Yan W, Adiconis X, Arnold ME, Lee JM, Levin JZ, Lin D, Wang C, Lieber CM, Regev A, He Z, Sanes JR. Single-Cell Profiles of Retinal Ganglion Cells Differing in Resilience to Injury Reveal Neuroprotective Genes. Neuron. 2019 Dec 18;104(6):1039-1055.e12. doi: 10.1016/j.neuron.2019.11.006. Epub 2019 Nov 26. PMID: 31784286; PMCID: PMC6923571.

Undale AH, Westendorf JJ, Yaszemski MJ, Khosla S. Mesenchymal stem cells for bone repair and metabolic bone diseases. Mayo Clin Proc. 2009 Oct;84(10):893-902. doi: 10.4065/84.10.893. PMID: 19797778; PMCID: PMC2755808.

Uruci S, Lo CSY, Wheeler D, and Taneja N (2021). R-Loops and Its Chro-Mates: The Strange Case of Dr. Jekyll and Mr. Hyde. Int. J. Mol. Sci. 22. 10.3390/ijms22168850.

Vaissière T, Sawan C, Herceg Z, Epigenetic interplay between histone modifications and DNA methylation in gene silencing, Mutation Research/Reviews in Mutation Research, Volume 659, Issues 1–2, 2008, Pages 40-48, ISSN 1383-5742,

Völkner M, Zschatzsch M, Rostovskaya M, Overall RW, Busskamp V, Anastassiadis K, Karl MO. Retinal organoids from pluripotent stem cells efficiently recapitulate retinogenesis. *Stem Cell Rep.* 2016;6:525–538. doi: 10.1016/j.stemcr.2016.03.001.

Wagstaff EL, ten Asbroek ALMA, ten Brink JB, et al. An alternative approach to produce versatile retinal organoids with accelerated ganglion cell development. Sci Rep. 2021;11:1101. doi: 10.1038/s41598-020-79954-8.

Wahle, P., Brancati, G., Harmel, C. *et al.* Multimodal spatiotemporal phenotyping of human retinal organoid development. *Nat Biotechnol* **41**, 1765–1775 (2023).

Wahlin, K.J., Maruotti, J.A., Sripathi, S.R. *et al.* Photoreceptor Outer Segment-like Structures in Long-Term 3D Retinas from Human Pluripotent Stem Cells. *Sci Rep* **7**, 766 (2017).

Wässle H. Parallel processing in the mammalian retina. Nat Rev Neurosci. 2004 Oct;5(10):747-57. doi: 10.1038/nrn1497. PMID: 15378035.

Wilson MH, Coates CJ, George AL Jr. PiggyBac transposon-mediated gene transfer in human cells. Mol Ther. 2007 Jan;15(1):139-45. doi: 10.1038/sj.mt.6300028. PMID: 17164785.

Yan W, Peng YR, van Zyl T, et al. Cell atlas of the human fovea and peripheral retina. *Sci Rep.* 2020;10:9802. doi: 10.1038/s41598-020-66092-9.

Young Young RW. Cell differentiation in the retina of the mouse. Anat Rec. 1985 Jun;212(2):199-205. doi: 10.1002/ar.1092120215. PMID: 3842042.

Yu J, Vodyanik MA, Smuga-Otto K, Antosiewicz-Bourget J, Frane JL, Tian S, Nie J, Jonsdottir GA, Ruotti V, Stewart R, Slukvin II, Thomson JA. Induced pluripotent stem cell lines derived from human somatic cells. Science. 2007 Dec 21;318(5858):1917-20. doi: 10.1126/science.1151526. Epub 2007 Nov 20. PMID: 18029452.

Zang, J., & Neuhauss, S. C. F. (2018). The Binding Properties and Physiological Functions of Recoverin. *Frontiers in Molecular Neuroscience*, 11, 473.

Zhao S, Jiang E, Chen S, Gu Y, Shangguan AJ, Lv T, Luo L, Yu Z. PiggyBac transposon vectors: the tools of the human gene encoding. Transl Lung Cancer Res. 2016 Feb;5(1):120-5. doi: 10.3978/j.issn.2218-6751.2016.01.05. PMID: 26958506; PMCID: PMC4758974.

Zhong, X., Gutierrez, C., Xue, T. *et al.* Generation of three-dimensional retinal tissue with functional photoreceptors from human iPSCs. *Nat Commun* **5**, 4047 (2014).

9. Statement on personal contributions

Unless otherwise stated, all experimental work presented in this dissertation was performed by me.

I generated the PiggyBac constructs, performed the nucleofection into the iPSC line, and maintained the resulting iPSC cultures.

The generation of ROs from the nucleofected cells was primarily carried out by Kritika Sharma (PhD student). The subsequent maintenance of these organoids was handled by undergraduate students Richa Joshi and Karla Vollmerig. I then utilized these ROs for all downstream experiments.

Specifically, I performed the RO tissue dissociation and subsequent flow cytometry analyses. I also conducted live cell imaging, all RNA isolations, cDNA syntheses, and RT-qPCR experiments, as well as the independent immunohistochemical staining and imaging.

Furthermore, I was solely responsible for data acquisition, processing, statistical analysis, and the interpretation of the results.

This dissertation was written entirely by me, without the involvement of co-authors. All figures and graphical illustrations were also created independently.

10. Acknowledgement

I would like to take this opportunity to express my heartfelt gratitude to everyone in the Busskamp group, as they have provided sufficient support and assistance throughout this project.

In particular, I would like to thank Prof. Dr. Volker Busskamp for allowing me to conduct such an interesting project in his laboratory. His guidance opened my horizon to many things and gave me experiences that were invaluable beyond the mundane atmosphere of the hospital.

I would also like to express my deep gratitude to the supervisors, Julia Pawlick, Kritika Sharma, and Marta Zucic, for their timely support, warm assistance, and excellent teaching. I would like to thank Julia and Marta for their invaluable support in molecular cloning and elicitation design, for supporting with insightful suggestions during the most difficult moments in cloning processes. I am also very grateful to Kritika, who helped me to cultivate the retinal organoids, optimize the experimental strategy, and taught me many useful skills during my work.

I would also like to thank the other members of the lab. In particular, I would like to thank Dr. Sarah Kunze for her smooth handling of all administrative tasks and Dr. Kirsten Harmening for her excellent supervision of our lab. I would like to thank Elizaveta Podoliak, Dr. Robert Prior, Dr. Rouhollah Habibey, and Johannes Striebel for their patience and help in overcoming many problems throughout the project. I would also like to thank Richa Joshi for her help with the media changes and Karla Vollmerig for preparing the necessary materials. Finally, I would like to express my deep appreciation to my parents, who have continuously provided me with the emotional support and encouragement that has been so vital to my growth throughout this journey.